

The Fundamental Plane of QSOs and the Relationship Between Host and Nucleus

Timothy S. Hamilton,^{1,2,3,4,5} Stefano Casertano,^{3,5} and David A. Turnshek^{2,5}

ABSTRACT

We present results from an archival study of 70 medium-redshift QSOs observed with the Wide Field Planetary Camera 2 on board the *Hubble Space Telescope*. The QSOs have magnitudes $M_V \leq -23$ (total nuclear plus host light) and redshifts $0.06 \leq z \leq 0.46$. The aim of the present study is to investigate the connections between the nuclear and host properties of QSOs, using high-resolution images and removing the central point source to reveal the host structure. We confirm that more luminous QSO nuclei are found in more luminous host galaxies. Using central black hole masses from the literature, we find that nuclear luminosity also generally increases with black hole mass, but it is not tightly correlated. Nuclear luminosities range from 2.3% to 200% of the Eddington limit. Those in elliptical hosts cover the range fairly evenly, while those in spirals are clustered near the Eddington limit. Using a principal components analysis, we find a kind of fundamental plane relating the nuclear luminosity to the size and effective surface magnitude of the bulge. Using optical nuclear luminosity, this relationship explains 96.1% of the variance in the overall sample, while another version of the relationship uses x-ray nuclear luminosity and explains 95.2% of the variance. The form of this QSO fundamental plane shows similarities to the well-studied fundamental plane of elliptical galaxies, and we examine the possible relationship between them as well as the difficulties involved in establishing this connection.

Subject headings: quasars: general — galaxies: active — galaxies: fundamental parameters

¹Research performed while a National Research Council Associate at NASA/GSFC

²Dept. of Physics & Astronomy, University of Pittsburgh, Pittsburgh, PA 15260, USA

³Space Telescope Science Institute, 3700 San Martin Drive, Baltimore, MD 21218, USA

⁴Present address: Shawnee State Univ., Dept. of Natural Sciences, 940 2nd St., Portsmouth, OH 45662

⁵email: thamilton@shawnee.edu, stefano@stsci.edu, turnshek@pitt.edu

1. INTRODUCTION

The availability of high-resolution, space-based imagery has been of great help to the study of QSOs and their host galaxies. Many low-to-medium redshift QSO hosts have been imaged with the Hubble Space Telescope in the past several years. At the same time, there has been a growing understanding of the workings of galactic nuclei and their central black holes. Magorrian et al. (1998) have found a proportionality between black hole and galactic spheroid masses in normal galaxies, and this has been refined by Kormendy & Gebhardt (2001), Häring & Rix (2004), and McLure et al. (2006). McLure & Dunlop (2001, 2002), Marconi & Hunt (2003), and Graham (2007) have studied this relation for active galaxies. Black hole mass has also been found to be related to the central stellar velocity dispersion (Ferrarese & Merritt 2000; Gebhardt et al. 2000; Tremaine et al. 2002; Ferrarese & Ford 2005; Bernardi et al. 2007). The velocity dispersion is itself tied to larger-scale galaxy properties through the fundamental plane of elliptical galaxies (Djorgovski & Davis 1987; Dressler et al. 1987). So there is now a wealth of evidence emerging on the individual relationships between large-scale properties of galaxies and those of their central regions.

In this paper we report on the connections between the nuclear and host properties of a large sample of low-redshift QSOs observed with the Wide Field and Planetary Camera 2 (WFPC2) on board the *Hubble Space Telescope* (*HST*). This follows our study of the QSO host luminosity function, described by Hamilton et al. (2002). We have collected and reanalyzed wide-band archival images of 70 QSOs with $M_V \leq -23$ mag (total nuclear plus host light) and redshifts $0.06 \leq z \leq 0.46$. This includes images taken by several teams, especially Bahcall et al. (1997), Hooper et al. (1997), Boyce et al. (1998), and McLure et al. (1999), among others. We have taken an inclusive approach in our sample selection, imposing no additional selection criteria on the QSOs besides those of total absolute magnitude and redshift. For each object we have subtracted the nuclear light component using two-dimensional image fits and have derived the luminosity and size of the underlying host galaxy by fitting an elliptical or disk-like light profile. A comparison of our results with other teams using the same data is given in §A.

We examine the host and nuclear luminosities in §3 and confirm earlier results that more luminous QSO nuclei are found in more luminous host galaxies. The range of host magnitudes is narrower than that of the nuclei, and we discuss possible selection effects. In §4, we compare literature estimates of central black hole masses with our nuclear and bulge luminosities. Nuclear luminosity generally increases with black hole mass, though there is not a strong correlation. Bulge luminosity shows little trend at all. We find the nuclear bolometric luminosities span a wide range of Eddington fractions, except among QSOs in spiral hosts, which cluster near the Eddington limit.

Using a principal components analysis, we demonstrate the existence of a fundamental plane connecting the nuclear luminosity to the host bulge’s size and effective surface magnitude (§5). This QSO fundamental plane can be found using either the optical or x-ray nuclear luminosities. The optical version explains 96.1% of the sample’s variance, and the x-ray version explains 95.2%. When we look at particular subsamples of QSOs, the plane tilts in different orientations, which are examined in §B.

Throughout this paper, we adopt a Friedmann cosmology with $H_0 = 50 \text{ km s}^{-1} \text{ Mpc}^{-1}$, $q_0 = 0.5$, and $\Lambda = 0$, to be in keeping with Hamilton et al. (2002). The effects on the results of assuming a more recent cosmology, $H_0 = 65 \text{ km s}^{-1} \text{ Mpc}^{-1}$, $\Omega_\Lambda = 0.7$, $\Omega_{\text{matter}} = 0.3$, are discussed in §5.2.

2. DATA

2.1. Sample

The sample is composed of 70 archival *Hubble Space Telescope* (*HST*) images of low-redshift QSOs. The selection criteria are that they have redshifts between $0.06 \leq z \leq 0.46$ and total (host plus nucleus) absolute magnitudes brighter than $M_V \leq -23$. Furthermore, they must have been observed with the *HST*’s Wide-Field Planetary Camera 2 (WFPC2), using broad-band filters, and have images publicly available in the *HST* archives as of 1999. This brings our sample to 70 QSOs.

Rather than restrict our study to a specific class of QSOs, we impose no physical criteria on the QSOs beyond those of magnitude and redshift. Thus we are able to study a broad range of properties and draw general conclusions.

2.2. Image Analysis

Even at *HST* resolution, the light of the unresolved nuclear central source significantly affects the extended light distribution of the host galaxy. A careful subtraction of the central point source is needed in order to measure the properties of the host accurately. The image reduction is described in detail by Hamilton et al. (2002). The following is a brief summary of the method, which is largely similar to that of Remy et al. (1997).

Because of the complex structure of the *HST* WFPC2 Point Spread Function (PSF), our analysis procedure has three principal steps: (1) A two-dimensional model of the PSF is fitted to the central point source, in order to determine its subpixel position and the telescope

focus, which affect the shape of the PSF. (2) The PSF and a galaxy model are simultaneously fitted to the entire image to distinguish the nuclear and host components. (3) The nuclear magnitude is determined from the PSF model. Then the fitted PSF is subtracted, and the magnitude of the host is determined from the residual light.

The model PSF is constructed from a set of artificial PSFs, created using the TinyTim software (the latest version is described by Krist & Hook 2004). Pixel sampling is important (especially for the Wide Field images) because in the shape of the response function, the PSF structure changes significantly, depending on both the telescope focus and on exactly how the point source is centered with respect to the pixel grid. For instance, a point source centered in the middle of a pixel will look different from one centered on a corner. If this centering is not accounted for, the model will not correctly apportion the light between the PSF and the extended source. The WFPC2 camera used for each observation is listed in Hamilton et al. (2002), Table 1.

The general PSF model is first fitted to the core of the QSO image, where the nuclear point source is the dominant feature, with the light of the extended galaxy treated as a constant background term. Saturated pixels and those affected by CCD “blooming” are masked from the fits. If the PSF is not saturated, we can achieve a precision of ≈ 0.1 pixels in the central position and $\approx 1\mu\text{m}$ in the focus position, for QSOs dominated by their nuclei. Our technique works in the presence of saturation, although the focus is determined less accurately. Once the position and focus have been found, a PSF of angular size large enough to cover the host image is created with these parameters, and it is used in the subsequent analysis.

A second two-dimensional fit distinguishes the light of the QSO from that of the resolved host galaxy, simultaneously fitting both parts. In this step, the model PSF’s brightness is scaled to match the QSO nuclear brightness, while a galaxy model is fitted to the host. The host model includes a simple morphological classification based on radial profile.

For spiral hosts with a visible bulge, we use an elliptical mask to fit the bulge and disk separately. The mask’s shape is determined by the QSO’s isophotal ellipticity and orientation. It exposes the region in which the bulge dominates the disk. The bulge+PSF is fitted first, using the mask. Next, the bulge model is subtracted from the entire image, and finally the disk is fitted. Bars and any other irregular components are not modeled; they have masks drawn by eye. This includes the irregularly-shaped bulges in PG 0052+251, MRK 1014, PG 1001+291, LBQS 1222+1010, and PG 1402+261. Of the regular bulges, we note that some are best modeled by a disk-like radial profile, while others are best fitted with an elliptical galaxy type profile.

Based on visual inspection, some hosts appear to have undergone recent, strong interactions that have severely distorted their appearance from those of a normal elliptical or spiral, and we have noted these in Table 1. The “interacting” category is rather subjective, and if seen at higher resolution, many others might have been classed this way.

Using the fitted parameters, we then subtract the properly scaled PSF from the QSO image, leaving the host galaxy. The magnitude of the nucleus is measured directly from the scaled PSF model. The host magnitude is measured from the PSF-subtracted image, within an aperture large enough to encompass the visible extent of the host. Outside the aperture, we extrapolate the host model to a radius of infinity and add this contribution to the light contained within the aperture, yielding the apparent magnitude of the host galaxy. The size of the host is represented by the half-light radius, $r_{1/2}$, in the case of ellipticals or the effective radius, r_{eff} , in the case of spirals. This parameter is taken directly from the fitted host model.

The absolute host and nuclear magnitudes are calculated as described in §3.3 of Hamilton et al. (2002); we briefly summarize the procedure here. From the filter magnitude measured above, we first obtain an apparent V magnitude by applying a color correction. Colors are taken from Cristiani & Vio (1990), for the nuclei, and from Fukugita et al. (1995), for the hosts. Cristiani & Vio (1990) use the Johnson filter set, so we convert the nuclear colors to the WFPC2 filters, using the IRAF SYNPHOT package and a power-law spectrum of the form $f_\nu = \text{constant}$. Once we have the apparent V magnitudes, the absolute V magnitudes are given by

$$M_V = m_V - 45.396 - 5 \log(1 + z - \sqrt{1 + z}) - K(V) - A_V , \quad (1)$$

where $K(V)$ is the V -band K-correction, and A_V is the Galactic extinction. Nuclear K-corrections are also taken from Cristiani & Vio (1990). For host K-corrections, we use the data of Pence (1976), which assumes no intrinsic reddening in the host galaxies. Galactic extinction, A_V , comes from Schlegel, Finkbeiner, & Davis (1998), by way of the Galactic extinction calculator on the NASA Extragalactic Database¹ (NED).

The error bars used in the plots and listed in Table 2 are the 1σ statistical uncertainties. In looking at the systematic errors, tests on simulated QSOs (including elliptical, disk, and disk+bulge hosts) show that we can recover their parameters rather well. In these tests, nuclear magnitudes are particularly accurate, with errors consistently less than 0.1 mag, and comparing favorably with the statistical uncertainties of ≈ 0.15 mag. Host magnitude errors are $\lesssim 0.2$ mag, extending a bit larger than the statistical uncertainties, which are typically

¹nedwww.ipac.caltech.edu

~ 0.1 mag. Effective surface magnitudes are generally off by ~ 0.2 mag arcsec $^{-2}$. The distribution of their statistical uncertainties peaks at ≈ 0.12 mag arcsec $^{-2}$. And the errors in log radius ($\log r_{1/2}$ or $\log r_{\text{eff}}$) are broadly distributed, almost all $\lesssim 0.02$, ranging a bit larger than the typical statistical error of ≈ 0.01 .

The effect of PSF convolution is probably the major source of error in these tests. Mathematically speaking, the light entering the telescope is first convolved with the telescope’s PSF and then binned into pixels. Our code convolves the host model with the PSF as it performs the fit, to better match the ideal, unconvolved parameters. But the effect of the finite aperture of the telescope is that some information is still lost. Simulations can show us systematic errors, but we can also look at systematic differences between our analysis method and those of other groups, simply by comparing our results. These are discussed in §A.

2.3. X-ray Luminosities

The x-ray luminosities, listed in Table 2 for a subset of the objects, are obtained from *ROSAT* and *Einstein* satellite data. For the *ROSAT* observations of Brinkmann et al. (1997) and Yuan et al. (1998), the data are provided as flux, $f_x[0.1, 2.4 \text{ keV}]$, in units of mW m $^{-2}$ integrated over the energy range 0.1–2.4 keV in the observer’s frame. Also listed is the energy spectral index, Γ , under the assumption of a power-law spectrum. With a spectrum of the form

$$f_\nu = A_x \nu^{\alpha_x} , \quad (2)$$

where A_x is a constant and $\alpha_x \equiv -(\Gamma - 1)$, then the constant of proportionality is

$$A_x = \frac{f_x [E_{\text{low}}, E_{\text{high}}] (1 + \alpha_x)}{\nu_{\text{high}}^{1+\alpha_x} - \nu_{\text{low}}^{1+\alpha_x}} , \quad (3)$$

where $E_{\text{low}} = 0.1$ keV, and $E_{\text{high}} = 2.4$ keV. The frequencies correspond to the energies as $\nu_{\text{high}} = 1000E_{\text{high}}/h$ (similarly for ν_{low}), where h is Planck’s constant. The luminosities, $\nu L_\nu |_{\nu_0}$, are evaluated at a rest-frame energy of $E_0 = 0.5$ keV (with $\nu_0 = 1000E_0/h$). The x-ray luminosity for PG 1229+204 comes from the PSPC-pointed *ROSAT* observation reported by Grupe et al. (2001). Reduction is performed as above, but over the 0.2–2.0 keV range.

For x-ray data from the *Einstein* satellite Imaging Proportional Counter (Wilkes et al. 1994; Margon et al. 1985), the energy range used is 0.16–3.5 keV. The luminosity of 3C 93 is calculated from the flux listed by Wilkes et al. (1994) for a spectral index of $\alpha_x \approx -1.5$, which is the closest to the average of our sample. Margon et al. (1985) actually provide the Q 2344+184 x-ray luminosity itself, in the format desired here, but they do not

quote a spectral index. Regardless of the source of data, we use the notation L_X for the nuclear x-ray luminosities in ergs s^{-1} , evaluated at the rest frame energy of 0.5 keV.

2.4. QSO Classifications

Radio-loudness classifications are collected primarily from Brinkmann et al. (1997) and Yuan et al. (1998), both of whom use a loudness criterion that classifies an object as radio-loud if it has a radio-to-optical flux density ratio in excess of 10. Radio-loudness classifications for the remaining objects come from a variety of sources, with extensive use made of the NASA Extragalactic Database.

In the analyses that follow, the QSO sample is subdivided into several categories, on the basis of radio-loudness and host morphology. We refer to radio-loud (L) and radio-quiet (Q) QSOs, as well as those with elliptical (E) or spiral (S) hosts. These categories are combined to describe radio-loud QSOs in elliptical hosts (LE), radio-louds in spiral hosts (LS), radio-quiet in elliptical hosts (QE) and radio-quiet in spiral hosts (QS). We note that the LS subsample has just four members, so it is omitted from many of the statistical analyses that follow. The more detailed morphological descriptions applied to some hosts in Table 1 (such as “interacting”) are not used in the analyses; only the E and S descriptions matter.

2.5. Redshift Effects

We find some redshift effects on the measured parameters. QSOs with nuclei much fainter than the hosts (up to 3.5 mag fainter) are only seen at low redshifts ($z < 0.3$). At high redshifts ($z \geq 0.3$), the nuclear absolute magnitudes do not get more than about 0.5 mag fainter than the host. The median effective surface magnitude (μ_e , described in detail in §5.1.2) brightens from 21.48 to 20.86 mag arcsec⁻² as we go to $z \geq 0.3$, and we see somewhat fewer faint hosts at high redshift, though the trend is not strong. We do not, however, see a trend in $\log r_{1/2}$ itself (when measured in kpc).

The uncertainties in host and nuclear magnitudes show no change with redshift. The uncertainties in $\log r_{1/2}$ and μ_e are larger, on average, for objects with redshift above 0.3. The median $\sigma_{\log r_{1/2}}$ rises from 0.007 (for $z < 0.3$) to 0.023 (for $z \geq 0.3$), while the median σ_{μ_e} rises from 0.10 to 0.14.

3. NUCLEAR VS. HOST LUMINOSITIES

3.1. Expectations

In addition to quantifying the behavior of nuclei and hosts separately, a major purpose for decomposing the QSO image into nuclear and host components is to look for relationships between the two. The correlations between nuclear and host parameters are important because they shed light on the interplay between the central engine and the galaxy that harbors it. One of the most straightforward questions is whether or not the nuclear and host luminosities are correlated.

In posing the question, we will assume the standard model of the central engine, a supermassive black hole surrounded by an accretion disk. Further assuming a fixed mass-to-light ratio for galaxies (following, for example, Jørgensen et al. 1996 and Magorrian et al. 1998), then the more massive a galaxy is, the more luminous it is. The mass of the galaxy includes not only stars but also gas, in the form of nebulae and a diffuse interstellar medium. Even in elliptical galaxies, which have a lower gas content than spirals, there can be gas in the form of a hot interstellar medium given off by the winds of post-main-sequence stars. Some of this gas (of both types) eventually accretes onto the central engine as fuel (Di Matteo et al. 2000), so a more luminous galaxy has more fuel available for the nucleus. Under Bondi accretion (Bondi 1952), the gas accretion rate onto the disk is proportional to the density of the gas far from the engine and to the square of the black hole mass, and the luminosity of the accretion disk is proportional to the accretion rate (Carter 1979). So given the model assumed here, a correlation between nuclear and host luminosities may naively be expected.

Earlier investigations have shown evidence of such a relationship. Hutchings et al. (1984) studied 78 QSOs and lower-luminosity Active Galactic Nuclei (AGN) out to a redshift of $z = 0.7$ and found a positive correlation between these parameters, suggesting that nuclear power is related to galaxy mass. McLeod & Rieke (1994a, b) used infrared H -band imaging of QSOs, in which band the ratio of nuclear to host luminosity is diminished. They considered two samples of low-redshift QSOs, one with low total (nucleus plus host) luminosities and one with high total luminosities, and they found that the hosts of the high-luminosity sample are brighter than those of the low-luminosity sample.

3.2. Analysis

The extinction-corrected absolute nuclear and host magnitudes are plotted against each other in Figure 1, with separate symbols for the LE, QE, LS, and QS categories. The object MS 2159.5–5713 is plotted as a separate symbol, because we do not know its radio-loudness.

The dotted curve in Figure 1 represents approximately the location of objects with a combined nuclear plus host magnitude of $M_V(\text{total}) = -23.0$, the faintest allowed under the conventional definition of a QSO and therefore the faint limit for our sample. The sample selection is made using published, ground-based data, so this limit is only approximate. The region in which the nuclear absolute magnitude is $M_V(\text{nuc}) > -23$ suffers from selection effects. We therefore perform the fits and correlation tests in this section only on those QSOs for which $M_V(\text{nuc}) \leq -23$.

3.2.1. Correlations and Functional Forms

The Spearman correlation coefficients for $M_V(\text{nuc})$ and $M_V(\text{host})$ are listed in Table 3. The overall correlation is not strong ($\rho = 0.350$), but we see greater correlations among radio-loud QSOs ($\rho = 0.578$) and especially among the 4 members of the LS subsample ($\rho = 0.800$). Unfortunately, the small number of LS QSOs makes it difficult to interpret this result.

We can also describe the data by fitting functional forms (Table 3). For this we use the “Bivariate Errors and intrinsic Scatter” (BES) estimator, described by Akritas & Bershadsky (1996). The BES method accounts for errors in both variables and is therefore useful in this application, for which there is not a perfectly-measured independent variable. The parameter $M_V(\text{nuc})$ is used as the independent variable because it has a larger range than $M_V(\text{host})$ does, even after restricting it to $M_V(\text{nuc}) \leq -23$.

The functional fit to the overall sample, shown as the solid line in Figure 1, can be expressed as

$$M_V(\text{host}) = (0.303 \pm 0.088)M_V(\text{nuc}) - (15.9 \pm 2.2) . \quad (4)$$

That is, host luminosity varies with nuclear luminosity as a power law with an exponent of 0.3. The slopes of most of the subsamples are similar to this, to within the errors. Those subsamples with especially low $M_V(\text{host})$ to $M_V(\text{nuc})$ correlations, QS and Q, are exceptions, as is the unreliable LS subsample.

3.3. Discussion

It appears from this analysis that QSOs with more luminous nuclei are slightly more likely to have more luminous hosts. The correlation itself is rather weak ($\rho = 0.350$) but unlikely to have occurred by chance (probability ≈ 0.008). The luminosity range we consider, $M_V(\text{nuc}) \leq -23$, is chosen to eliminate the stronger selection effects.

3.3.1. Selection Effects

The extremely narrow range of $M_V(\text{host})$ as compared to $M_V(\text{nuc})$ is partly due to the sample selection, with objects being selected to have a combined $M_V(\text{nuc} + \text{host}) \leq -23$. But even when just the $M_V(\text{nuc}) \leq -23$ region is examined, the range of magnitudes spanned by the hosts (3.1 mag) is smaller than the range spanned by the nuclei (4.2 mag).

If we instead used all of the objects lying outside the $M_V(\text{nuc} + \text{host}) \leq -23$ line (rather than $M_V(\text{nuc}) \leq -23$), our $M_V(\text{nuc})$ vs. $M_V(\text{host})$ fit would be slightly flatter (slope=0.24), but within $1\text{-}\sigma$ of our results here. The subsample slopes would show a similar change, except for the radio-louds, which aren't affected (they only exist at higher nuclear luminosities). The Spearman correlation would be stronger (from $\rho = 0.350$ to 0.451). The radio-loud subsamples, again, would not be affected. But all of the others would be strengthened, except for the QE's, which weaken (from $\rho = 0.394$ to 0.191). The correlations might be even stronger if fainter classes of AGN (those with $M_V(\text{nuc} + \text{host}) > -23$) were included, but they are outside the scope of this study.

There may be objects missing from the region of Figure 1 with high host luminosity and low nuclear luminosity (the upper left corner), due to sample selection effects. Optical searches for QSOs have typically stipulated that objects have a “stellar appearance” on photographic plates. The dominance of the host here might keep this an empty region in optically-selected QSO samples, but it is not a problem for x-ray and radio-selected samples.

This study uses archival data from a variety of *HST* proposals and, therefore, a mix of QSO selection methods. These are noted in Table 1. From the proposals and published articles by the original proposers, we have determined that only one object, PG 1229+204, was chosen for its lack of an extended host in ground-based images. An additional 13 QSOs were chosen from optically-selected catalogs, most commonly the Palomar-Green (PG) survey (Schmidt & Green 1983). Another 9 QSOs were chosen from the Large Bright Quasar Survey (LBQS), which is optically selected but has safeguards to prevent the rejection of objects with detectable “fuzz” surrounding the nucleus (Foltz et al. 1987). The remaining 47 QSOs in the sample were originally observed with *HST* for reasons that do not have

direct optical biases. This includes radio- and x-ray-selected QSOs. For those QSOs that appear in multiple *HST* proposals that were available for this study, we place them in the most “unbiased” category their proposals permit. The QSOs proposed for or selected in ways most likely to be biased against the upper left corner of Figure 1 therefore number 14 out of 70 (those marked with “B” or “C” in Table 1). Most of these 14 QSOs have nuclei that are more luminous than their host galaxies and tend to lie on the right-hand side of Figure 1, as expected. (And so there is little overlap with those 14 QSOs that are fainter than the $M_V(\text{nuc}) \leq -23$ cut.) But two of them have approximately equal host and nuclear luminosities (PG 1229+204 and PHL 1093), and US 3498 has a nucleus 3.3 magnitudes less luminous than its host.

As for the effects of these potentially biasing QSOs on the $M_V(\text{nuc})$ – $M_V(\text{host})$ correlation, we note that the farthest outliers in the upper-right corner of Figure 1 are not among the 14 biased QSOs. Furthermore, the sample of radio-loud QSOs includes only 2 such biased objects, and the correlation between $M_V(\text{nuc})$ and $M_V(\text{host})$ is actually stronger for that sample.

3.3.2. *Technical Comparison with Other Studies*

Other space-based studies have examined the relationship between host and nuclear luminosity, as well. We present the technical details of their observations and analysis methods here, but we will defer a comparison with their results until §6.1.

Bahcall et al. (1997) use the WFPC2 on *HST* to study a sample of 20 QSOs with redshifts $z \leq 0.3$ and total absolute magnitudes in the range $-24.4 \leq M_V \leq -27.1$. All of these QSOs are included in our sample. Observations of four different stars are used for PSFs. The nucleus is subtracted from each image using both 1- and 2-dimensional methods, with the 2-D results being adopted in the end. In the 2-D method, the PSF is subtracted from the QSO first, with each of the four stars being tried in turn, and the one which leaves the fewest residuals being adopted. A host model is then fitted to the residual image.

Dunlop et al. (2003) also use the WFPC2 on *HST* to study a sample of 10 radio-loud QSOs and 13 radio-quiet QSOs with redshifts $0.1 \leq z \leq 0.25$. All of their QSOs are included in our sample except for 5 objects (3 radio-louds and 2 radio-quiet) whose images were not publicly available when we defined our sample and began analysis. Stellar observations are used to create a PSF that is subtracted from the QSO images using 2-dimensional modeling, with the host model being fitted simultaneously with the scaled PSF.

Another study using *HST*’s WFPC2 is that of O’Dowd et al. (2002), who analyze the

host and nuclear luminosities of 40 BL Lacs and 22 radio-loud QSOs with redshifts between $0.015 \lesssim z \lesssim 0.5$. They perform a simultaneous host plus PSF fit to the radial profiles of the BL Lacs. For the QSOs, they use the published results from other studies and therefore mostly overlap our sample.

4. NUCLEAR LUMINOSITY AND ITS RELATION TO BLACK HOLE MASS

4.1. Black Hole Mass

Black hole masses have been variously estimated using $H\beta$ line widths, galaxy bulge masses, and stellar velocity dispersions, among other methods, since they cannot be measured directly. There are problems with applying some of these methods to QSOs, given their great distances and the glare from the nuclear emission. Not all are convinced by such methods, and it is with these caveats that we adopt the following black hole masses from the literature. But while the mass measurements themselves are subject to these systematic uncertainties, their use by other researchers does permit us to make self-consistent comparisons of their QSO results with ours.

Magorrian et al. (1998) study black holes in nearby, normal galaxies. Using *HST* photometry and ground-based spectroscopy, they model the stellar orbital velocities for given mass-to-light ratios and black hole masses. With the assumption that the black hole mass is proportional to bulge mass, they find that $\mathcal{M}_{\text{BH}} = 0.005\mathcal{M}_{\text{bulge}}$, where \mathcal{M}_{BH} represents the black hole mass and $\mathcal{M}_{\text{bulge}}$ is the bulge mass. More recently, other groups (Kormendy & Gebhardt 2001; Marconi & Hunt 2003; McLure et al. 2006) have used improved measurements to revise the black hole to bulge mass ratio downward to

$$\mathcal{M}_{\text{BH}} \sim 0.002\mathcal{M}_{\text{bulge}} . \tag{5}$$

Häring & Rix (2004) find evidence of a non-linear relationship, but their average ratio agrees with this value.

Without assuming that this sort of relation holds true for QSOs, we have taken the black hole masses for 26 of our QSOs from McLure & Dunlop (2001) and list these in Table 4. They calculate the masses from the QSOs' $H\beta$ line width, a method that assumes the line width comes from the Doppler-broadened motion of clouds around the black hole. This method requires knowing the size of the Broad-Line Region (BLR), which they calculate from the relation of Kaspi et al. (2000).

The results of McLure & Dunlop (2001) come from a combination of published data

and new spectral observations. We do not undertake independent calculations of the black hole masses from the variety of published line widths and BLR sizes because, as stressed by Laor (1998), published values of $H\beta$ for the same QSO often vary greatly from one study to another. McLure & Dunlop (2001) have original $H\beta$ observations for nearly half of their sample, make their calculations in a consistent manner, and demonstrate care where they add literature data to their own observations, making sure that these aren't likely to introduce large systematic errors. We use their black hole masses for those reasons and because of the large overlap (26 objects) between their sample and the QSOs in our study. As they list no uncertainties for the black hole masses, we adopt the high-end estimate of Vestergaard (2004) for this method, 0.4 dex. This 1σ uncertainty is larger than what we can obtain by propagating the known uncertainties.

4.2. Eddington Limit

We would also like to know if these QSOs are radiating at close to their theoretical limits. The Eddington limit for the bolometric emission from the nucleus is given by (McCray 1979)

$$L_{\text{Edd}} \simeq 1.3 \times 10^{38} \frac{\mathcal{M}_{\text{BH}}}{\mathcal{M}_{\odot}} \text{ erg sec}^{-1} . \quad (6)$$

We calculate the bolometric luminosities from $M_V(\text{nuc})$ (listed in Table 1), using the data from Elvis et al. (1994), who provide the ratios between different monochromatic luminosities, νL_ν , and the bolometric luminosity, L_{bol} (their Table 17). For the V -band,

$$\left\langle \frac{\nu L_\nu}{L_{\text{bol}}} \right\rangle = 14.2 \pm 5.1 , \quad (7)$$

where νL_ν is evaluated at $\nu = 5.45 \times 10^{14}$ Hz, corresponding to a wavelength of $\lambda = 5500 \text{ \AA}$, the central wavelength of the V filter.

We obtain L_ν from our calculated $M_V(\text{nuc})$, which are Vega-system magnitudes, using the zeropoints and photometric conversions of Voit (1997). In terms of $M_V(\text{nuc})$,

$$\log f_\nu = -0.4 [M_V(\text{nuc}) + 48.62] , \quad (8)$$

where f_ν is the V -band flux density per unit frequency, in units of $\text{erg cm}^{-2} \text{ s}^{-1} \text{ Hz}^{-1}$.

The V -band luminosity density, L_ν , is then calculated from f_ν and the QSO's redshift, z . Since $M_V(\text{nuc})$ is already K-corrected, then no further cosmological correction needs to be applied, and the luminosity density is obtained from the simple geometric relation,

$$L_\nu = 4\pi d^2 f_\nu , \quad (9)$$

where d is the distance. The bolometric luminosity can then be calculated from Table 17 of Elvis et al. (1994). The nuclear luminosity and the black hole mass can be used together to determine the Eddington fraction, $L_{\text{bol}}/L_{\text{Edd}}$, listed logarithmically in Table 4. Since the errors in nuclear magnitude are much smaller than those assumed for the black hole masses, the propagated errors in $\log(L_{\text{bol}}/L_{\text{Edd}})$ all come out to be 0.4. Beaming of the nuclear emission would create further uncertainties. We discuss this effect later.

As our calculated Eddington fractions depend on the black hole mass estimates of §4.1, the same caveats apply here. There could also be some problems in using the luminosity ratios of Elvis et al. (1994). Energies above 10 keV are not included in the bolometric luminosity, due to the unknown spectrum in that region at the time of the paper. More important is the estimate of the “Big Blue Bump” in the UV-optical region. As pointed out by Mushotzky (1997), later X-ray studies (Laor et al. 1997; Zheng et al. 1997) have indicated that the continuum flux in this region is lower than some earlier estimates and parameterizations (Mathews & Ferland 1987). However, Elvis et al. (1994) are not cited in this discussion, and though their mean spectrum has a gap between approximately 1000 Å and 0.1 keV, they may avoid this problem because they do have data for the optical region and therefore do not have to parameterize there.

4.3. Results

4.3.1. Bulges and Black Holes

Out of the 26 QSOs that have black hole masses given by McLure & Dunlop (2001), we have modeled, spheroidal bulges for 20, whose absolute magnitudes are given in Table 4. We restrict consideration to the spheroidal (elliptical) bulges, as opposed to those that have disk-like profiles, because they are more likely to have a dynamical relationship between their bulge and black hole (Kormendy 2001). In Figure 2, the bulge magnitudes, $M_V(\text{bulge})$, are plotted against the black hole masses. Figure 2 also shows the slope of any relationship like equation (5). If the QSO black holes have masses that are a constant fraction of the bulge mass, the distribution will lie parallel to this line. Assuming a constant mass-to-light ratio, then if black hole mass is a fixed fraction of bulge mass, an increase of one decade in black hole mass will correspond to an increase in one decade in bulge luminosity, or 2.5 magnitudes.

There is a great deal of scatter in the distribution of bulge magnitude with black hole mass. The two parameters show only a weak anticorrelation overall (Table 3), just $\rho = -0.263$. Radio-quiet objects, on the other hand, show a stronger anticorrelation, $\rho = -0.594$,

and in particular, the 7 QE objects have a tight anticorrelation at $\rho = -0.847$, which can be seen from Figure 2.

The BES fits to the data are listed in Table 3. The overall fit can be expressed in the form

$$M_V(\text{bulge}) = (-1.43 \pm 1.18) \log(\mathcal{M}_{\text{BH}}/\mathcal{M}_{\odot}) - (10.5 \pm 10.5) . \quad (10)$$

The slopes of most of the subsamples are similar, to within the errors, with the notable exceptions of the spiral and QS categories. This is not really parallel to equation (5), which would have a slope of 2.5 in this figure. The scatter is quite large, and they are about one standard deviation different.

4.3.2. Nuclear Luminosities and Eddington Fractions

A plot of the nuclear luminosity vs. black hole mass is presented in Figure 3. The distribution of $M_V(\text{nuc})$ vs. $\log \mathcal{M}_{\text{BH}}$ shows that there is a very general trend of luminosity increasing with mass. The Spearman correlations, given in Table 3, include a fairly weak anticorrelation overall, with $\rho = -0.378$. The spiral subsample in this case shows the strongest anticorrelation, with $\rho = -0.667$. Note that we have 26 objects to study in this analysis, because we do not impose any restrictions on the bulges, as we did in §4.3.1.

The fits are listed in Table 3. The overall fit to the data is given by

$$M_V(\text{nuc}) = -(1.98 \pm 1.16) \log(\mathcal{M}_{\text{BH}}/\mathcal{M}_{\odot}) - (6.90 \pm 10.2) , \quad (11)$$

but it suffers from outlying points. The spiral and QS subsamples show positive slopes, with the spirals having 2.09 ± 2.19 .

The distribution of log Eddington fractions is presented in Figure 4, both for the complete sample and broken down by subclass. The bin width is 0.4, which is equal to the uncertainties. In general, the QSOs demonstrate a wide range in their Eddington fractions, extending from $-1.6 \leq (\log L_{\text{bol}}/L_{\text{Edd}}) \leq 0.3$. Two objects (3C 273 and PG 1402+261) appear to have luminosities above the Eddington limit, but they exceed it by less than the uncertainties. PG 1302–102, with $\log L_{\text{bol}}/L_{\text{Edd}} = 0.0$, is also placed in the highest bin.

We can see that the objects in spiral hosts tend to have higher Eddington fractions, -0.8 to 0.3 (in the logarithm), while those in elliptical hosts are spread across -1.6 to 0.2 (again in the logarithm). No distinction is apparent between the Eddington fractions of radio-loud and radio-quiet objects.

4.4. Discussion

4.4.1. *Bulges and Black Holes*

We cannot say much about a fixed black hole to bulge mass ratio, such as equation (5). While it appears from Figure 2 that there might be some weak correlation between the bulge magnitude and the black hole mass, the details of the relationship are hidden by the large uncertainties in the masses. The range of masses is not much larger than their uncertainties, allowing for a wide range of possible slopes, so the results are simply inconclusive. That the 7 QE objects form the tightest correlation is interesting. Since there are not many objects in this category, not too much can be drawn from this result yet, but it presents an avenue for follow-up studies.

4.4.2. *Nuclear Luminosities and Eddington Fractions*

We see that as black hole mass increases, the QSO’s nuclear luminosity also increases (Figure 3), although the trend is rather weak. A stronger trend might naively be expected, as the more massive black holes have higher Eddington limits. Yet the QSOs do not all radiate near their limits (Figure 4), although there is a clear division according to host morphology. Those in spiral hosts do tend to cluster at relatively high Eddington fractions and only go as low as 16% of Eddington. But those in elliptical hosts are more evenly distributed over a wider range, extending as low as 2.5% of Eddington. The difference may be caused by spirals typically having smaller black holes.

5. THE “FUNDAMENTAL PLANE” OF QSOS

Instead of only looking at correlations of two parameters at a time, we can analyze multiple dimensions at once. Principal Components Analysis (PCA) provides a convenient method for identifying and examining multidimensional correlations. We use this method to search for further connections between the nuclear and host properties.

5.1. Analysis and Results

5.1.1. Restricted Sample

For our PCA, we use a restricted sample of those QSOs for which we have all of the following parameters: $M_V(\text{nuc})$, L_X , $r_{1/2}$, and μ_e , where μ_e is the effective surface magnitude of the galactic bulge. We further require that each QSO have a modeled, spheroidal bulge (the entire galaxy, in the case of elliptical hosts). These qualifications restrict the sample to the 42 QSOs listed in Table 2.

In order to prevent the choice of units from artificially weighting some parameters more than others, each parameter is first normalized by subtracting its mean and dividing by its variance. The PCA is then performed on these normalized variables. Note that the normalization for each of the subsamples is carried out separately from the others. In the output, each of the eigenvectors is written as a linear combination of the original (but normalized) parameters. The eigenvalues are scaled so that the sum of all eigenvalues equals the total number of eigenvectors (and therefore the total number of parameters as well).

5.1.2. Effective Surface Magnitude

There is already a well-studied fundamental plane (FP) for normal, elliptical galaxies (Djorgovski & Davis 1987; Dressler et al. 1987) that incorporates galaxy size, $r_{1/2}$, central velocity dispersion, σ_c , and effective surface magnitude, μ_e . Here we define μ_e as the surface magnitude (expressed in magnitudes arcsec⁻²) of an elliptical galaxy or bulge at a distance $r_{1/2}$ from the center of the galaxy. Note that there is another form of effective surface magnitude, $\langle\mu\rangle_e$, which is the average surface magnitude within the half-light radius. These two forms are related such that $\mu_e - \langle\mu\rangle_e = 1.39$ (van Albada et al. 1993). We can derive an expression for μ_e by first noting that the total host luminosity in counts, L_{host} (corresponding to the absolute magnitude, $M_V(\text{host})$), of a spheroidal galaxy following an $r^{1/4}$ profile and extended out to an infinite radius can be expressed as

$$L_{\text{host}} = \kappa_L e^{7.67} I(r_{1/2}) r_{1/2}^2 (1 - \epsilon) , \quad (12)$$

where $I(r_{1/2})$ is the galaxy’s surface brightness (in count-rate per unit area) at the half-light radius, $r_{1/2}$, and ϵ is the ellipticity of the isophotes. Then κ_L is a constant, which we calculate numerically as $\kappa_L = 0.01054$. Note that Malkan (1984) gives an expression for L_{host} that leads to $\kappa_L = 0.01058$, a difference of only 0.4%.

Converting to magnitudes arcsec⁻², we obtain

$$\mu_e = M_V(\text{host}) + 2.5 \log [\theta_{1/2}^2 \kappa_L e^{7.67} (1 - \epsilon)] \quad , \quad (13)$$

where $\theta_{1/2}$ is the half-light radius expressed in arc seconds. In the case of an elliptical bulge, we substitute $M_V(\text{bulge})$ in place of $M_V(\text{host})$. We can now look for a QSO fundamental plane that involves the host parameters, $\log r_{1/2}$ and μ_e , as well as a measure of the nuclear luminosity, $M_V(\text{nuc})$ or $\log L_X$. In this, we use the effective surface magnitude, rather than the bulge magnitude, so that we can make direct comparisons between our results and the well-studied fundamental plane of elliptical galaxies.

5.1.3. PCA Results and Derivation of the QSO Fundamental Plane

We can perform two PCAs, an optical one using $M_V(\text{nuc})$, $\log r_{1/2}$, and μ_e as the parameters, and an x-ray one that uses $\log L_X$ for the nuclear luminosity. From the optical PCA performed on this sample of 42 objects, we find that 96.1% of the variance can be explained with just the first two eigenvectors (\mathbf{e}_1 and \mathbf{e}_2), and the QSOs mostly lie in a plane within this parameter space. This we consider to be a fundamental plane for QSOs. For the corresponding x-ray results, the first two eigenvectors explain 95.2% of the variance in the sample, and we find here an x-ray QSO fundamental plane. See Table 5 for the individual eigenvalues.

We obtain the formula for the optical fundamental plane of the full sample,

$$M_V(\text{nuc}) = -77.5 + 3.14\mu_e - 14.2 \log r_{1/2} \quad . \quad (14)$$

The x-ray fundamental plane for the full sample is

$$\log L_X = 79.3 - 2.03\mu_e + 8.74 \log r_{1/2} \quad . \quad (15)$$

Views of the optical and x-ray fundamental planes, with the QSO data points superimposed, are displayed in Figure 5. Note that the host properties describe the horizontal and the nuclear luminosity the vertical in this plot.

The same analysis can also be made of the separate QSO subsamples. We save the mathematics and analysis details for §B but discuss the results in more general terms in §5.2 and §6.4, below. We find that, indeed, the subsamples are individually distributed into planes, with their first two eigenvectors accounting for about as much variance as in the full sample. Some of the subsample planes, however, differ in orientation.

5.1.4. Precision

The precision of the fundamental plane can be judged from the percentage of the variance explained by the third eigenvector, as listed in Table 5. The third eigenvector describes the scatter perpendicular to the plane.

We can obtain another measure of the fundamental plane’s errors by comparing the measured nuclear luminosities with the values we calculate from the QSO FP. This can be done when solving for any of the FP’s three variables in terms of the other two. The Pearson correlation coefficients and the root-mean-squared differences between the actual values and their fundamental plane solutions are listed in Table 6. The Pearson correlation coefficient is useful for accounting for the size of the error, relative to the range of the variable.

It is clear from these results that the QSO FP has both the smallest root-mean-square (RMS) errors and the highest correlation with the data when it is solved for the host galaxy size, $\log r_{1/2}$. The full-sample fundamental plane in this form is

$$\log r_{1/2} = -0.0704M_V(\text{nuc}) + 0.221\mu_e - 5.46 \quad (16)$$

for the optical, or

$$\log r_{1/2} = 0.114 \log L_X + 0.232\mu_e - 9.07 \quad (17)$$

for the x-ray. The measured host sizes are plotted against the fundamental plane in Figure 6.

5.1.5. Effect of Statistical Errors

The effect of the sample’s statistical errors on the measurement of the QSO fundamental plane can be tested by creating an artificial FP, adding errors, and trying to recover the FP using the PCA method described above. In this test, we first create a fake QSO FP equation. We then randomly place 42 objects within the limits of $\log r_{1/2}$ and μ_e covered by the 42 real QSOs of the PCA sample. Each object’s nuclear luminosity ($M_V(\text{nuc})$ or $\log L_X$) is calculated from the fake FP equation. We next add errors to each data point in the following way.

The measurement uncertainties for each QSO are listed in Table 2, and we use them to throw the errors. For each object in the fake FP, we use the uncertainties from a different QSO of the actual sample. The error for a given parameter is thrown randomly, according to a two-sided Gaussian of width equal to the QSO’s uncertainty. The parameter value for the fake object is then shifted by this random error. In this way, the fake QSO FP is scrambled to simulate measurement errors.

We then run a Principal Components Analysis on the fake, scrambled FP. After we derive the equation for it, we compare this with the equation we used to create the fake dataset in the first place. Using this technique, we not only test the actual optical and x-ray QSO FPs, but we also vary their coefficients. This lets us find out whether the statistical errors push the measured QSO FP into a particular direction. Starting from the QSO FPs in the form of equations (14) and (15), we individually vary the coefficients of $\log r_{1/2}$ and μ_e , replacing them with values 0.5, 1, and 2 times their actual amounts. It turns out that the statistical errors do not greatly affect the measured angle of the QSO FP, regardless of how we vary the equation’s coefficients. The coefficients “recovered” from the scrambled data are always within 2% of their assigned values and in most cases are within 1%.

5.2. Discussion

The existence of the QSO fundamental plane shows that there is a strong link between a QSO’s host and nuclear properties, although we cannot make a claim as to cause and effect. We find that the QSO subsamples have their own fundamental planes and that there is a great difference in their slopes (we specifically refer to the gradient). Mathematically, the FP gradients calculated in §B describe the size of the dependence of the nuclear luminosity on the features of the host. A large gradient, as in the x-ray form of the radio-quiet sample, means that a small change in the host size or effective surface magnitude is associated with a large change in the nuclear luminosity. Because the FP is a function of two parameters, looking only at the gradient obscures the details of this relationship somewhat. But it is useful in that it demonstrates the underlying similarity between the FPs of the different subsamples, a similarity that is not obvious from looking at the individual equations. Geometrically, the different planes act almost as a single plane that pivots about its principal axis, changing its angle relative to the host ($\log r_{1/2}, \mu_e$) plane. That is, the gradients of most of the subsamples point along the same (or opposite) azimuth, and the major difference between their FPs is the magnitude of their gradients. More interestingly, not only does the gradient change magnitude, but it even reverses direction in some cases. In the optical FPs, only the QE sample slopes in the direction opposite the rest. In the x-ray FPs, all of the radio-quiet samples (Q, QE, and QS) exhibit this behavior. In fact, if we rank the planes by their gradients, radio-loudness seems to have the biggest influence in how the subsamples are grouped.

The statistical errors in the final PCA dataset do not appear to affect the measured orientation of the QSO FP significantly. While this does not itself discount the possibility that systematic errors could have an effect, we note the difference between the FPs of the

radio-loud ellipticals (LE) and radio-quiet ellipticals (QE). These two FPs have slopes of opposite sign, but they deal with hosts of the same morphology. Thus systematic errors from the image fitting procedure are unlikely to create the QSO FPs artificially. While they might still influence the measured slope, they are not enough to cover up these large differences between the subsample FPs. In addition to statistical and modeling errors, the nuclear luminosity is affected by QSO variability. This is another source of FP thickness.

Finally, we have adopted a Friedmann cosmology with $H_0 = 50 \text{ km s}^{-1} \text{ Mpc}^{-1}$, $q_0 = 0.5$, and $\Lambda = 0$ to be in keeping with Hamilton (2001) and Hamilton et al. (2002). A more currently-accepted cosmology might have $H_0 = 65 \text{ km s}^{-1} \text{ Mpc}^{-1}$, $\Omega_{\text{matter}} = 0.3$, and $\Omega_{\Lambda} = 0.7$. The fundamental plane variables can be converted into this cosmology for each individual QSO, but the inclusion of a non-zero cosmological constant makes the conversions depend on redshift.

The differences are smallest for QSOs at the high-redshift end of the sample. Converting to the updated cosmology lowers the values of $\log r_{1/2}$ by 0.101, for QSOs at the low-redshift limit of $z = 0.06$, and it lowers them by 0.039, for QSOs at the high-redshift limit of $z = 0.46$. The conversion makes the magnitudes, $M_V(\text{nuc})$ and μ_e , fainter by 0.505 to 0.195 mag, and it lowers $\log L_X$ by 0.202 to 0.007 (again, the low-redshift changes are listed first). These changes are small compared to the ranges of the variables. More importantly, they do not produce any significant effect in the QSO fundamental plane quality. In the optical case, the percentage of the sample variance explained by the PCA would be lowered from 96.1% to 95.6%, and in the x-ray case, from 95.2% to 94.7%.

6. DISCUSSION

6.1. Host and Nuclear Luminosity

We have shown that host luminosity shows a shallow increase with nuclear luminosity. Some relationship of this type is expected because in more massive (and therefore more luminous) hosts, there is more gas available to fuel the supermassive black hole thought necessary to power a QSO.

Bahcall et al. (1997) do not find convincing evidence in their results of a significant correlation between host and nuclear luminosities, and they do not provide a fitted relation, noting that much of the apparent correlation in their Figure 8 comes from 3C 273, the brightest object in their sample.

O’Dowd et al. (2002) find a shallow but statistically significant trend of host luminosity

increasing with nuclear luminosity. For the combined sample, host luminosity increases by 1 mag or less (depending on beaming corrections for the BL Lacs) for each 7 mag increase in nuclear luminosity. Their study uses a mixed sample of objects (BL Lacs and QSOs).

For their radio-loud QSOs, Dunlop et al. (2003) find a shallow relationship, $M_R(\text{host}) = +0.114(\pm 0.15)M_R(\text{nuc}) - 20.98(\pm 3.72)$. For radio-quiet QSOs, they find a nearly-flat relationship, $M_R(\text{host}) = -0.018(\pm 0.18)M_R(\text{nuc}) - 23.73(\pm 4.29)$, when they reject the two lowest-luminosity objects as not being true QSOs. Overall, they report that both results are consistent with there being no correlation, using the Spearman rank correlation test.

6.2. Bulge Luminosity and Black Hole Mass

Without interpreting the weak bulge and black hole result too far, we note for comparison that our fitted relation, equation (10), is fairly consistent with that derived by McLure & Dunlop (2001). It corresponds to their equation (3), after transforming their M_{RC} to M_V with the elliptical galaxy colors from Fukugita et al. (1995). However, their newer results with an expanded sample (McLure & Dunlop 2002) find a steeper slope than our equation (10). We should also note that a reanalysis of their data by Graham (2007), editing the sample and using a different linear regression method, steepens it to almost twice our slope. Graham finds close agreement between this and his similar reanalysis of Marconi & Hunt (2003).

Neither McLure & Dunlop nor Marconi & Hunt restrict themselves only to QSOs, and so they have samples extending to much lower black hole masses than ours, which improves their correlations. The problem with looking at a QSO population alone, as we do, is that the short range of masses is not much greater than the measurement errors. More data are needed for QSOs with less massive black holes, if true QSOs even exist with much smaller masses. And the real test will come when the uncertainties in black hole mass measurements have been reduced.

6.3. Nuclear Luminosities and Eddington Fractions

We see that nuclear luminosity generally increases with black hole mass, although the trend is not strong. Some kind of relationship might be expected, since the gravity of the black hole is the ultimate energy source for the QSO. For instance, as black hole mass increases, more material can be trapped by its gravity and be pulled into the accretion disk; the faster material accretes onto the disk, the more the disk heats up and light is produced.

But any effect produced by this is rather weak.

We can see some trends, though, when we look at the Eddington fractions of the QSOs. The QSOs in spirals tend to be radiating at higher Eddington fractions than those in ellipticals. While spirals generally have lower nuclear luminosities, they also tend to have smaller black holes. This could be a result of the amount of gas available to fuel the QSO. If there is a fixed rate of gas flowing into the vicinity of the black hole, owing to the shape of orbits in the galactic bulge, then it may be that a smaller black hole, with a lower Eddington limit, is able to capture enough material to keep it radiating near its limit. But as the black hole grows, although it is able to capture more of the material orbiting near it, there is not enough available to keep it near the increased Eddington limit. It could also simply be that if, rather than limiting ourselves to traditionally-defined QSOs, we were to include lower-luminosity Seyfert galaxies in our sample, we might find them populating the low Eddington fraction region of the spiral host plot.

A criticism of one of the trends described above comes from Woo & Urry (2002), who suggest that what appears to be a correlation between black hole mass and nuclear luminosity might be explained by sample selection effects. They argue that there is not sufficient evidence for a correlation, because the lack of objects in the lower right side of Figure 3 is due to the exclusion of lower-luminosity AGN from the sample. They state that radio galaxies, for instance, can have low nuclear luminosity but high black hole mass. The exclusion from our sample of radio galaxies might not have exactly the same effect on our distributions as it does for Woo & Urry (2002), since they include radio galaxies but are not able to obtain good bolometric measurements for the least luminous ones. The upper left side of the plot is real, however, because of the Eddington limit.

Finally, we should also say that there is an added uncertainty from QSO variability and the possible beaming of the nuclear emission. For instance, PG 1302-102 is variable (Eggers, Shaffer, & Weistrop 2000 show changes of about 0.2 mag), and its correlated optical and radio structure could indicate beaming (Hutchings et al. 1994b). There should be little beaming among the radio-quiet. But among the radio-louds, it could exaggerate some nuclear luminosities and Eddington fractions.

6.4. Fundamental Plane

The fundamental plane for QSOs shows a relationship between the nuclear and host features that goes beyond the simple correlation of nuclear and host luminosities. This behavior may be connected to other, known relations between the objects, such as the

fundamental plane of normal, elliptical galaxies. The fundamental plane for elliptical galaxies involves the galaxy’s size, effective surface magnitude, and stellar velocity dispersion. It varies quantitatively for galaxies in different environments and for observations in different wavebands, but one measurement in the V -band (Scodreggio et al. 1998) is

$$\log r_{1/2} = 1.35 \log \sigma_c + 0.35 \mu_e + \text{Constant}, \quad (18)$$

where σ_c is the galaxy’s central velocity dispersion.

Although the ratio of the coefficients of the half-light radius to the effective surface magnitude is different from the QSO fundamental plane, there is a formal similarity between the QSO and normal FPs, which might point to a link between the host galaxy’s central velocity dispersion and the nuclear luminosity of the QSO. It is therefore tempting to try to derive the QSO fundamental plane directly from the elliptical galaxy fundamental plane, but we find two problems with this approach, both arising from the relation of black hole mass to nuclear luminosity.

By applying the correlation between the central velocity dispersion in elliptical galaxies and the mass of their central black hole, we can put the elliptical galaxy fundamental plane, equation (18), in terms of black hole mass. We use the formula of Merritt & Ferrarese (2001),

$$\mathcal{M}_{BH} = 1.3 \times 10^8 \left(\frac{\sigma_c}{200 \text{ km s}^{-1}} \right)^{4.72} \mathcal{M}_\odot. \quad (19)$$

Further substituting in equation (11) to put this in terms of nuclear luminosity, we obtain

$$\log r_{1/2} = -0.14 M_V(\text{nuc}) + 0.35 \mu_e + \text{Constant}. \quad (20)$$

This is our attempt to derive the QSO optical fundamental plane from the normal galaxy FP, and we see that it differs from the actual QSO FP, equation (16).

The coefficient we derive for $M_V(\text{nuc})$ in the above equation depends upon the exponent of the velocity dispersion in equation (19) and on the slope of equation (11). Different studies have found exponents for the velocity dispersion (a hotly debated topic) that range from about 3.75–5.1 (Ferrarese & Merritt 2000; Gebhardt et al. 2000; Tremaine et al. 2002; Ferrarese & Ford 2005; Bernardi et al. 2007), and the slope of equation (11) has a large uncertainty. But we still cannot make the coefficient of $M_V(\text{nuc})$ in equation (20) match that of the QSO optical fundamental plane. Deriving the QSO fundamental plane directly from the normal galaxy FP would require a steep dependence of $M_V(\text{nuc})$ upon $\log(\mathcal{M}_{BH}/\mathcal{M}_\odot)$, which we do not find.

We can attempt to derive the x-ray QSO fundamental plane the same way, using the correlation between the x-ray luminosities and black hole masses in our sample. A linear

fit using the BES method (in keeping with the derivation for the optical plane) gives us $\log L_X = 2.77 \log (\mathcal{M}_{\text{BH}}/\mathcal{M}_{\odot}) + 19.8$. This would lead to

$$\log r_{1/2} = 0.10 \log L_X + 0.35 \mu_e + \text{Constant} \quad (21)$$

as our attempted derivation, which is close to the actual x-ray QSO FP. The use of x-ray luminosities normalized to 0.5 keV glosses over the complexities of QSO spectra, providing only a first glimpse of the x-ray QSO fundamental plane. Follow-up analysis should account for the different spectral features of the individual QSOs and should use luminosities of a higher energy band.

There is both an interesting property and a problem in the QSO FP orientations, which we detail in §B. As we change from one QSO class to another, the fundamental plane essentially pivots about an axis, so the differences between the subsamples are mostly reduced to a single dimension, the slope (or gradient) relative to the μ_e - $\log r_{1/2}$ plane. Some subsample FPs even slope in the opposite direction from the overall FP. This creates another problem for deriving the QSO FPs (whether optical or x-ray) from the normal galaxy fundamental plane. These opposite slopes are not reflected in our fits of nuclear luminosity against black hole mass, and the poor correlation of these two quantities lies in contrast with the relatively thin QSO fundamental plane. This points to our need for a better understanding of the proper relationship between nuclear luminosity and black hole mass.

Because the QSO FP mathematically describes a link between the host and the nucleus, its slope might depend on the physical nature of the link. It would be interesting to find if the different QSO FP orientations described in §B come about from different fueling mechanisms that might be found in the various subsamples. We see, for instance, that radio-quiet and radio-loud QSOs are characterized by very different slopes in their x-ray FPs, but the understanding of what makes these QSO types differ is still too limited to speculate further here. In our ongoing research, we are expanding the fundamental plane study to other types of AGN, such as Seyferts. We can then compare their FP orientations with those of the different QSO subsamples, which may teach us more about the physics underlying the QSO fundamental plane.

7. CONCLUSIONS

1. QSO hosts cover a much smaller range of luminosity than do their nuclei. We find a relatively weak trend between host and nuclear luminosities.

2. Host bulge luminosities do not show a significant correlation with $H\beta$ -derived black hole masses, but a Magorrian-type relationship cannot be ruled out.

3. The correlations seen among nuclear luminosity, black hole mass, and Eddington fraction are subject to selection effects from the exclusion of lower-luminosity AGN.

4. We show that there is a strong, 3-parameter relationship between host and nuclear properties. The nuclear luminosity, size of the host, and effective surface magnitude of the host together form a plane in which most of the QSOs lie. This fundamental plane for QSOs explains 96.1% of the variance in the sample, in its optical form, and 95.2% in its x-ray form. While this plane shows some similarities to the fundamental plane for elliptical galaxies, we do not find a clear, analytical derivation from one to the other.

This research has been supported through a National Research Council Associateship at NASA’s Goddard Space Flight Center, as well as through a Graduate Student Fellowship and a grant from the Director’s Discretionary Research Fund, both from the Space Telescope Science Institute. We made use of the following databases: the HST data archive; NASA/IPAC Extragalactic Database (NED), operated by the Jet Propulsion Laboratory, California Institute of Technology, under contract with the National Aeronautics and Space Administration; and NASA’s Astrophysics Data System Abstract Service. We would like to thank George Djorgovski for his comments on the interpretation of the fundamental plane. We are also grateful for the long support and encouragement of the late Elizabeth K. Holmes, a National Research Council Associate at JPL.

A. COMPARISON WITH OTHER QSO IMAGING RESULTS

An idea of the systematic differences between our analysis method and others is gotten by comparing our QSO imaging results with those of other researchers using the very same data sets (Table 7). The most useful comparisons are of the nuclear and host apparent magnitudes, as well as the host effective radius. We include only those results that can be directly compared with ours—those reporting the apparent WFPC2 filter magnitudes in the Vega magnitude system.

As discussed in §2.2 and more extensively by Hamilton et al. (2002), we first match the focus and the PSF sub-pixel center and then apply a simultaneous nucleus and host fit. Our host magnitudes are measured from the PSF-subtracted image, with the host model used to fill in masked pixels and to extrapolate beyond the aperture to infinite radius. There are several objects, flagged in Table 7, whose host sizes are difficult to compare, but which we have included nonetheless. These are generally spiral hosts with both a bulge (or bar) and a disk, which the literature analysis treats as having only a single component. We either model both the bulge and the disk, or we mask one component and fit only the other. In

either case, our magnitudes reflect the total host magnitude, but the radius (taken directly from the model) represents only one component. See the table notes for the details.

Next are particular comparisons with the groups with which we share several objects. Closely matching our results are those of McLure et al. (1999), which are often within 0.1 mag of ours. They use a similar technique, a simultaneous nucleus and host fit to the 2-D image, that differs from ours in the specifics of the PSF and host models. The close correspondence of our results argues for a robustness in the approach. The size scales of our host galaxies are, on average, about 1.2 (± 0.3) times larger than those fitted by McLure et al. (1999), ignoring those objects flagged in Table 7 where we have fitted models to different components of the host. Note that although the apparent magnitudes are listed as Cousins R , they are, in fact, in the $F675W$ filter. McLure says that the $R_C - F675W$ color conversions for these objects turned out to be too small to make a difference.

Larger differences, on the other hand, can be seen between our results and those of Bahcall et al. (1997) and Boyce et al. (1998). Their analysis methods are quite different from ours. Bahcall et al. (1997) progressively subtract a stellar nucleus until the residual profile turns over in the center, then fit a host model to the remaining light. We compare with their 2-D model results. In principle, this method should somewhat overestimate the host magnitude. Boyce et al. (1998) fit simultaneous nucleus and host models using the cross-correlation method described by Boyce, Phillipps, & Davies (1993). Host magnitudes are measured directly from the light remaining after PSF subtraction. All of their images are marred by saturation in the innermost pixels, which they remove entirely from the analysis and set to null for the host magnitude calculation. Thus their host magnitudes are upper limits, as they state.

Lastly, Hooper et al. (1997) use the same cross-correlation method as Boyce et al. (1998), although they apparently take the host magnitudes from the models, rather than from the PSF-subtracted images. They report their results in the Johnson R filter, rather than the WFPC2 $F675W$ in which they were taken (stated to be a < 0.15 mag conversion), and they apply other magnitude corrections (≤ 0.1 mag). The conversions are color-dependent, and the corrections are not explicitly given, so we have left these in Johnson R . Sizeable differences with our results can be seen, but the magnitude differences should be treated as rough.

B. SUBSAMPLE FUNDAMENTAL PLANES

B.1. Subsample Forms

In addition to the full sample, we also look for fundamental planes in the individual QSO subsamples; their PCA eigenvalues are presented in Table 8. As before, the subsamples are labeled “L” for radio-loud QSOs, “Q” for radio-quiet, “E” for those in elliptical hosts, and “S” for those in spirals. Because the restricted sample includes only a single radio-loud QSO in a spiral host, there is no separate FP for the “LS” subsample.

We find that, indeed, the subsamples are individually distributed into planes, and the third eigenvalue (representing scatter perpendicular to the plane) in each case is about as small as the full sample’s. Table 9 lists the coefficients for the subsamples’ fundamental plane equations. The equations are presented in the optical case as $M_V(\text{nuc}) = R_{\text{coeff}} \log r_{1/2} + M_{\text{coeff}} \mu_e + C$ and in the x-ray case as $\log L_X = R_{\text{coeff}} \log r_{1/2} + M_{\text{coeff}} \mu_e + C$, where R_{coeff} and M_{coeff} are coefficients, and C is a constant. The orientations of some of these planes are clearly different from the others.

B.2. Gradients

The situation is more easily described geometrically, because it turns out that their biggest differences can be characterized by a single parameter, the slope (magnitude of the gradient). To visualize the relationship among the planes, let us imagine a 3-D plot similar to Figure 5, but rescaled, replacing $M_V(\text{nuc})$ with $M_V(\text{nuc})/2.5$ and μ_e with $\mu_e/2.5$, so that all quantities are pure logarithms. This will allow a more straightforward comparison of lengths and angles. For the vertical axis (\mathbf{k}), we will use the nuclear luminosity ($\log L_X$ or $M_V(\text{nuc})/2.5$), the \mathbf{i} axis will be $\log r_{1/2}$, and the \mathbf{j} axis will be $\mu_e/2.5$. Again, the host properties describe the horizontal and the nuclear luminosity the vertical.

In the following, let us represent the rescaled QSO fundamental plane by the function $F = F(\log r_{1/2}, \mu_e/2.5)$. The gradient of the fundamental plane is $\nabla F = (\partial F / \partial \log r_{1/2}) \hat{\mathbf{i}} + [\partial F / \partial (\mu_e/2.5)] \hat{\mathbf{j}}$, where $\hat{\mathbf{i}}$ and $\hat{\mathbf{j}}$ are unit vectors. Note that since F is a plane, its gradient is the same at any point we choose to evaluate it. We can look at the magnitude and direction of the gradient, where the magnitude is given by

$$\|\nabla F\| = \left\{ \left(\frac{\partial F}{\partial \log r_{1/2}} \right)^2 + \left[\frac{\partial F}{\partial (\mu_e/2.5)} \right]^2 \right\}^{1/2}, \quad (\text{B1})$$

and the direction (azimuth, the angle counterclockwise from the $+i$ axis) is given by

$$\alpha = \arctan \left[\frac{\partial F / \partial (\mu_e / 2.5)}{\partial F / \partial \log r_{1/2}} \right]. \quad (\text{B2})$$

These gradients are listed in Table 10. The full sample is listed first, while the subsamples are grouped according to general azimuth and then ranked in order of gradient magnitude. The subsample gradients tend to point either along the same azimuth as the overall FP or in the opposite direction (180° away from it). This near-uniformity in azimuth lies in contrast with the wide range of magnitudes (from 6.45 to 65.9), and so the gradient magnitudes seem to be the distinguishing feature between the subsample planes.

It should not be surprising that the azimuths are nearly uniform, as the first principal axis of the PCA follows roughly the Kormendy relation (Kormendy 1977) between μ_e and $\log r_{1/2}$. What is interesting, then, is the large degree of freedom for the planes about this axis.

B.3. Discussion

The x-ray FPs have an interesting symmetry in their gradients. We see the the L and Q classes are paired with each other in having the largest gradients (except for the S class, discussed below) but pointing in opposite directions. This opposition in gradient directions is followed by the mixed classes, with the LE plane on one side and the QE and QS planes on the other. Note that the LS class is too small to derive a separate fundamental plane for it. The S class is an exception to this symmetry. For the PCA sample, the only difference between the S and QS populations is a single object, 3C 351, which is radio-loud and apparently spiral. With the small populations of these two classes, this one QSO makes a real difference. In general, we find that the various planes for radio-loud objects point in one direction, while those for radio-quiet objects point in the opposite direction.

The optical FPs all have approximately the same azimuth, with the exception of the QE class, which points in the opposite direction. But even among the optical planes, there are distinct groupings (mostly by radio-loudness) that almost mirror those of the x-ray FPs. Aside from the QE class, the spirals and radio-quiet objects have the largest gradients, while the ellipticals and radio-loud objects have the smallest. It seems that radio loudness makes the greatest difference in the gradient and azimuth, both in the x-ray and the optical FPs, while the host morphology appears to be less important.

REFERENCES

- Akritas, M. G., & Bershad, M. A. 1996, *ApJ*, 470, 706
- Bahcall, J. N., Kirhakos, S., & Saxe, D. H. 1997, *ApJ*, 479, 642
- Bernardi, M., Sheth, R. K., Tundo, E., & Hyde, J. B. 2007, *ApJ*, 660, 267
- Blandford, R. 1999, in *ASP Conf. Ser. 182, Galaxy Dynamics*, ed. D. R. Merritt, M. Valluri, & J. A. Sellwood (San Francisco: ASP), 87
- Bondi, H. 1952, *MNRAS*, 112, 195
- Boyce, P. J., Disney, M. J., Blades, J. C., Boksenberg, A., Crane, P., Deharveng, J. M., Macchetto, F. D., Mackay, C. D., & Sparks, W. B. 1998, *MNRAS*, 298, 121
- Boyce, P. J., Phillipps, S., & Davies, J. I. 1993, *A&A*, 280, 694
- Brinkmann, W., Yuan, W., & Siebert, J. 1997, *A&A*, 319, 413
- Carter, B. 1979, in *Active Galactic Nuclei*, ed. C. Hazard & S. Mitton (Cambridge: Cambridge Univ. Press), 185
- Cristiani, S. & Vio, R. 1990, *A&A*, 227, 385
- Di Matteo, T., Quataert, E., Allen, S. W., Narayan, R., & Fabian, A. C. 2000, *MNRAS*, 311, 507
- Disney, M. J., Boyce, P. J., Blades, J. C., Boksenberg, A., Crane, P., Deharveng, J. M., Macchetto, F., Mackay, C. D., Sparks, W. B., & Phillipps, S. 1995, *Nature*, 376, 150
- Djorgovski, S., & Davis, M. 1987, *ApJ*, 313, 59
- Dressler, A., Lynden-Bell, D., Burstein, D., Davies, R. L., Faber, S. M., Terlevich, R. J., Wegner, G. 1987, *ApJ*, 313, 42
- Dunlop, J. S., McLure, R. J., Kukula, M. J., Baum, S. A., O’Dea, C. P., & Hughes, D. H. 2003, *MNRAS*, 340, 1095
- Eggers, D., Shaffer, D. B., & Weistrop, D. 2000, *AJ*, 119, 460
- Elvis, M., et al. 1994, *ApJS*, 95, 1
- Fabian, A. C. 1999, *MNRAS*, 308, L39

- Ferrarese, L., & Merritt, D. 2000, *ApJ*, 539, L9
- Ferrarese, L., & Ford, H. 2005, *Space Sci. Rev.*, 116, 523
- Foltz, C. B., Chaffee, F. H., Jr., Hewett, P. C., MacAlpine, G. M., Turnshek, D. A., Weymann, R. J., Anderson, S. F. 1987, *AJ*, 94, 1423
- Fukugita, M., Shimasaku, K., & Ichikawa, T. 1995, *PASP*, 107, 945
- Gebhardt, K., et al. 2000, *ApJ*, 539, 13
- Graham, A. W. 2007, *MNRAS*, in press (arXiv:0705.0618)
- Grupe, D., Thomas, H.-C., & Beuermann, K. 2001, *A&A*, 367, 470
- Hamilton, T. S. 2001, PhD thesis, Univ. of Pittsburgh
- Hamilton, T. S., Casertano, S., & Turnshek, D. A. 2002, *ApJ*, 576, 61
- Håring, N., & Rix, H. 2004, *ApJ*, 604, 89
- Hooper, E. J., Impey, C. D., & Foltz, C. B. 1997, *ApJ*, 480, 95
- Hutchings, J. B., Crampton, D., & Campbell, B. 1984, *ApJ*, 280, 41
- Hutchings, J. B., Holtzman, J., Sparks, W. B., Morris, S. C., Hanisch, R. J., & Mo, J. 1994a, *ApJ*, 429, 1
- Hutchings, J. B., Morris, S. C., Gower, A. C., & Lister, M. L. 1994b, *PASP*, 106, 642
- Jørgensen, I., Franx, M., & Kjærgaard, P. 1996, *MNRAS*, 280, 167
- Kaspi, S., Smith, P. S., Netzer, H., Maoz, D., Jannuzi, B. T., & Giveon, U. 2000, *ApJ*, 533, 631
- Kirhakos, S., Bahcall, J. N., Schneider, D. P., & Kristian, J. 1999, *ApJ*, 520, 67
- Kormendy, J. 1977, *ApJ*, 218, 333
- Kormendy, J. 2001, in *ASP Conf. Ser. 230, Galaxy Disks and Disk Galaxies*, ed. J. G. Funes & E. M. Corsini (San Francisco: ASP), 247
- Kormendy, J., & Gebhardt, K. 2001, in *AIP Conf. Proc. 586, 20th Texas Symposium on Relativistic Astrophysics* (Melville: AIP), 363

- Krist, J., & Hook, R. 2004, *The Tiny Tim User's Guide*, (Baltimore: STScI), <http://www.stsci.edu/software/tinytim/tinytim.pdf>
- Laor, A. 1998, *ApJ*, 505, 83
- Laor, A., Fiore, F., Elvis, M., Wilkes, B., & McDowell, J. 1997, *ApJ*, 477, 93
- Magorrian, J., et al. 1998, *ApJ*, 115, 2285
- Malkan, M. A. 1984, *ApJ*, 287, 555
- Marconi, A., & Hunt, L. K. 2003, *ApJ*, 589, 21
- Margon, B., Downes, R. A., Chanan, G. A. 1985, *ApJS*, 59, 23
- Mathews, W., & Ferland, G. 1987, *ApJ*, 323, 456
- McCray, R. 1979, in *Active Galactic Nuclei*, ed. C. Hazard & S. Mitton (Cambridge: Cambridge Univ. Press), 227
- McLeod, K. K., & Rieke, G. H. 1994a, *ApJ*, 420, 58
- McLeod, K. K., & Rieke, G. H. 1994b, *ApJ*, 431, 137
- McLure, R. J., & Dunlop, J. S. 2001, *MNRAS*, 327, 199
- McLure, R. J., & Dunlop, J. S. 2002, *MNRAS*, 331, 795
- McLure, R. J., Kukula, M. J., Dunlop, J. S., Baum, S. A., O'Dea, C. P., & Hughes, D. H. 1999, *MNRAS*, 308, 377
- McLure, R. J., Jarvis, M. J., Targett, T. A., Dunlop, J. S., & Best, P. N. 2006, *MNRAS*, 368, 139
- Merritt, D., & Ferrarese, L. 2001, *ApJ*, 547, 140
- Mushotzky, R. F. 1997, in *ASP Conf. Ser. 128, Mass Ejection from Active Galactic Nuclei*, ed. N. Arav, I. Shlosman, & R. J. Weedman (San Francisco: ASP), 141
- O'Dowd, M., Urry, C. M., & Scarpa, R. 2002, *ApJ*, 580, 96
- Pence, W. 1976, *ApJ*, 203, 39
- Remy, M., Surdej, J., Baggett, S., & Wiggs, M. 1997, in *1997 HST Calibration Workshop*, ed. S. Casertano et al. (Baltimore: STScI), 374

- Schlegel, D. J., Finkbeiner, D. P., & Davis, M. 1998, *ApJ*, 500, 525
- Schmidt, M., & Green, R. F. 1983, *ApJ*, 269, 352
- Scodreggio, M., Gavazzi, G., Belsole, E., Pierini, D., & Boselli, A. 1998, *MNRAS*, 301, 1001
- Silk, J., & Rees, M. J. 1998, *A&A*, 331, L1
- Tremaine, S., et al. 2002, *ApJ*, 574, 740
- van Albada, T. S., Bertin, G., & Stiavelli, M. 1993, *MNRAS*, 265, 627
- Vestergaard, M. 2004, in *ASP Conf. Ser. 311, AGN Physics with the Sloan Digital Sky Survey*, ed. G. Richards & P. Hall (San Francisco: ASP), 69
- Voit, M., ed. 1997, *HST Data Handbook, Vol. I (Version 3.0; Baltimore: STScI)*
- Wilkes, B. J., Tananbaum, H., Worrall, D. M., Avni, Y., Oey, M. S., & Flanagan, J. 1994, *ApJS*, 92, 53
- Woo, J.-H., & Urry, C. M. 2002, *ApJ*, 579, 530
- Yuan, W., Brinkmann, W., Siebert, J., Voges, W. 1998, *A&A*, 330, 108
- Zheng, W., Kriss, G., Telfer, R., Grimes, J., & Davidsen, A. F. 1997, *ApJ*, 475, 469

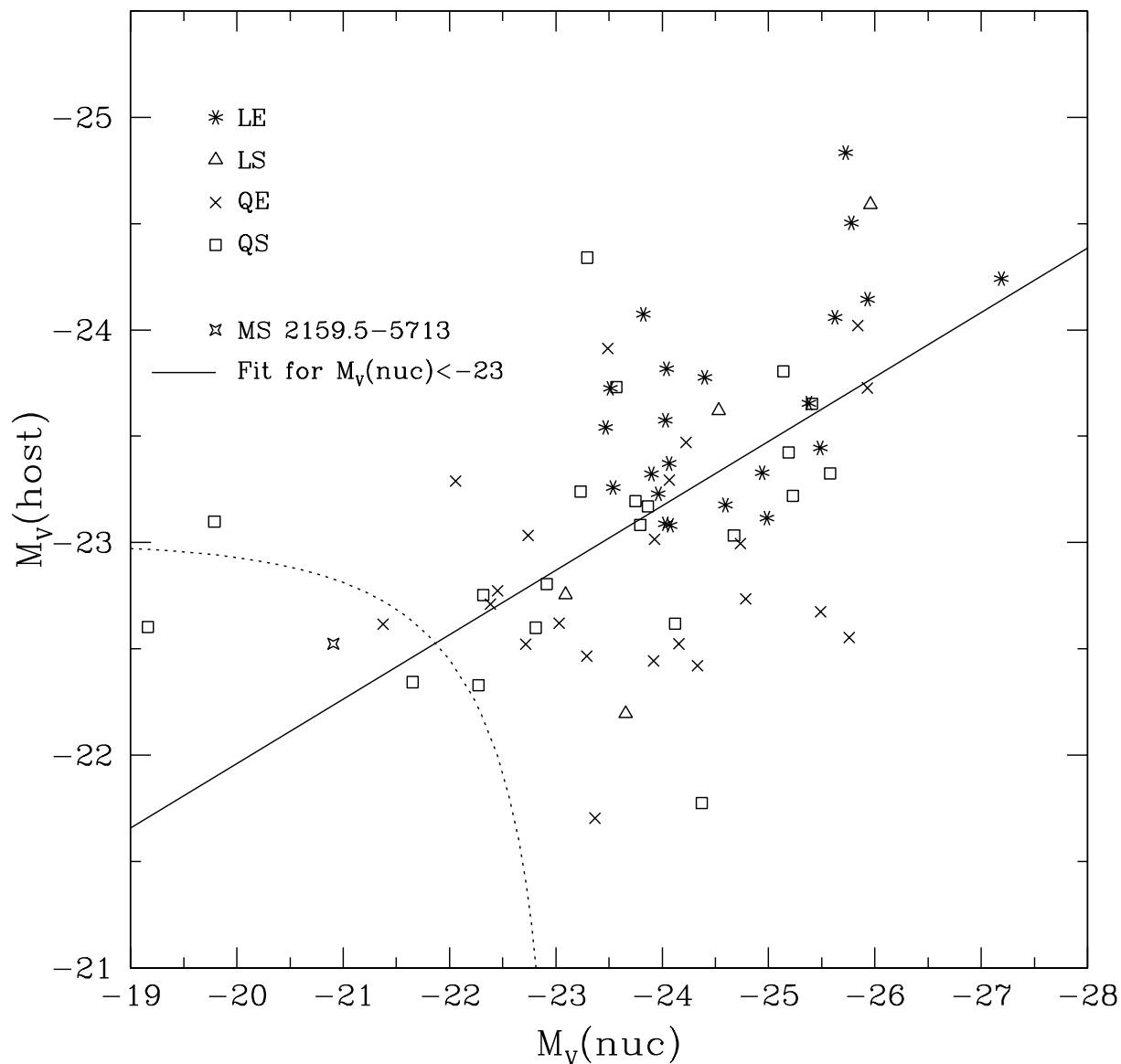


Fig. 1.— Overall distribution of host and nuclear luminosities. The QSOs are marked as radio-loud (L) or quiet (Q) and with elliptical (E) or spiral (S) hosts. The dotted curve is the approximate bound for objects with total (nucleus plus host) magnitude of $M_V(\text{total}) > -23$. The solid line is fitted to those QSOs with nuclear luminosity $M_V(\text{nuc}) \leq -23$ to avoid any bias by the few objects with fainter nuclei.

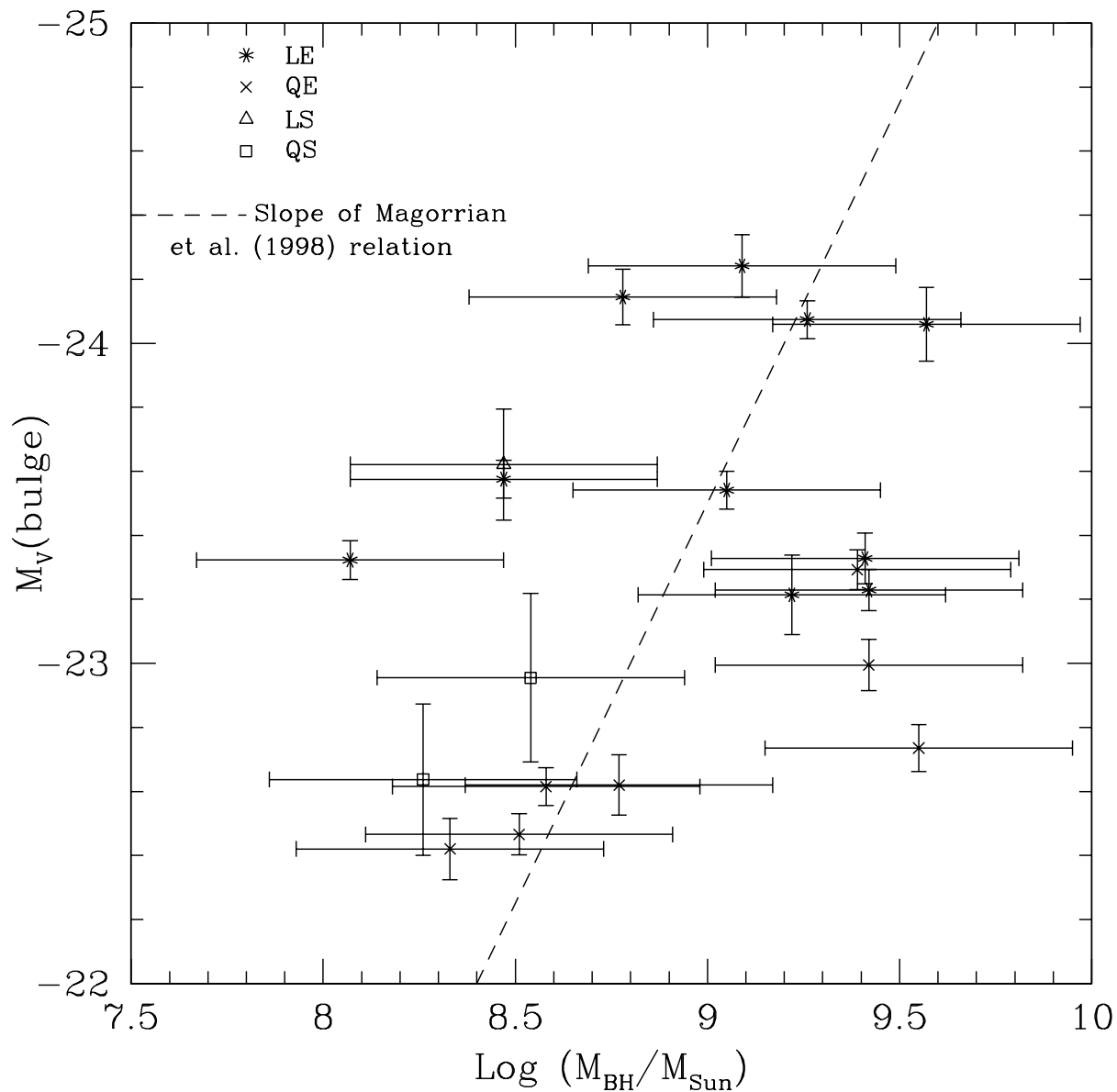


Fig. 2.— Bulge absolute magnitude vs. black hole mass. Objects with disk-like or unmodeled bulges are not included in the plot. The dashed line is not a fit but is drawn parallel to the relation of Magorrian et al. (1998). The correlation is weak and, given the large errors in the masses, does not resolve the question of a black hole to bulge mass relation.

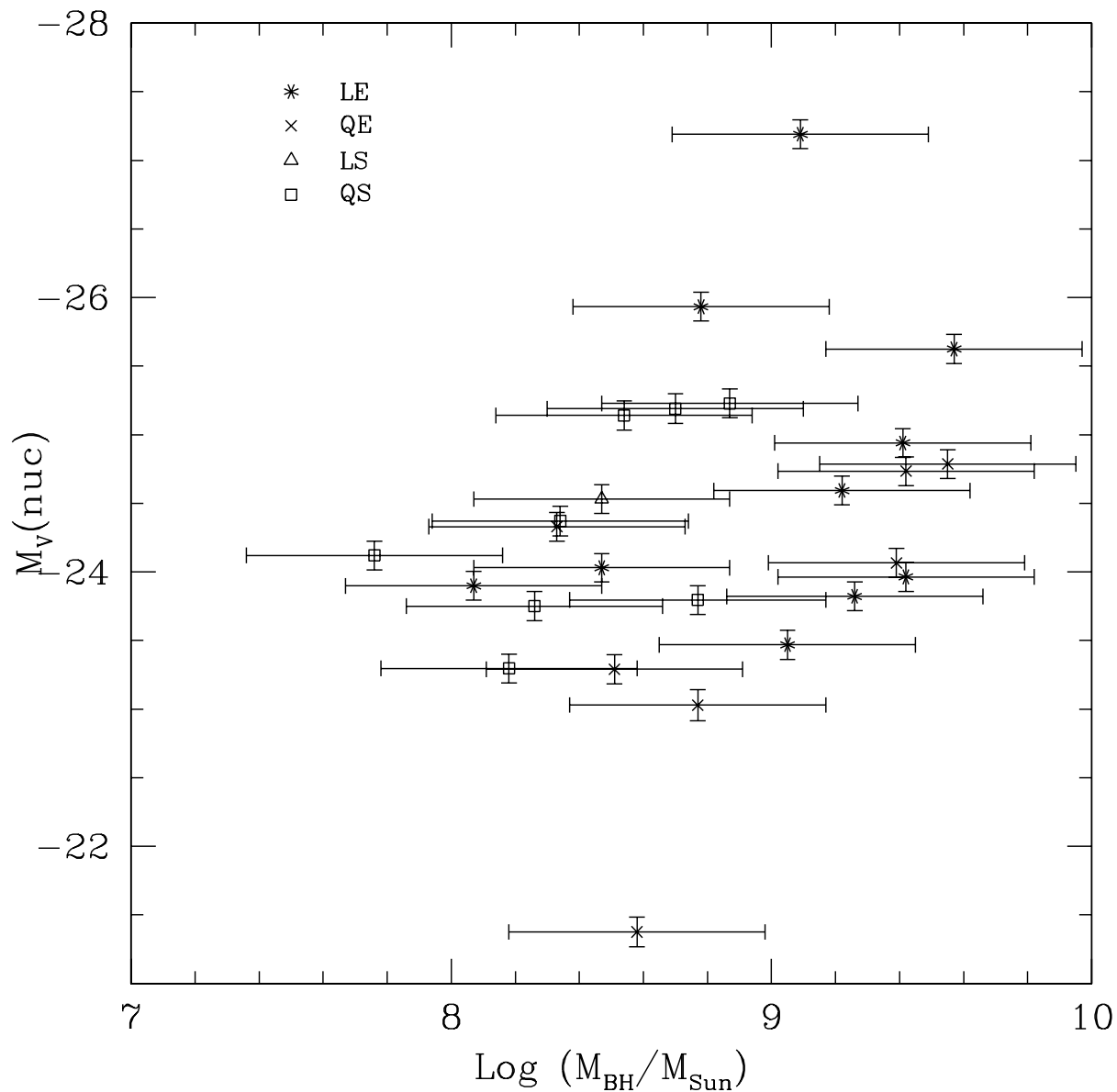


Fig. 3.— Nuclear absolute magnitude vs. black hole mass. Nuclear luminosity generally increases with greater black hole mass, though the correlation is low. The lack of QSOs in the upper left corner is due to the Eddington limit, and there might be selection effects responsible for the lack of objects in the lower right corner.

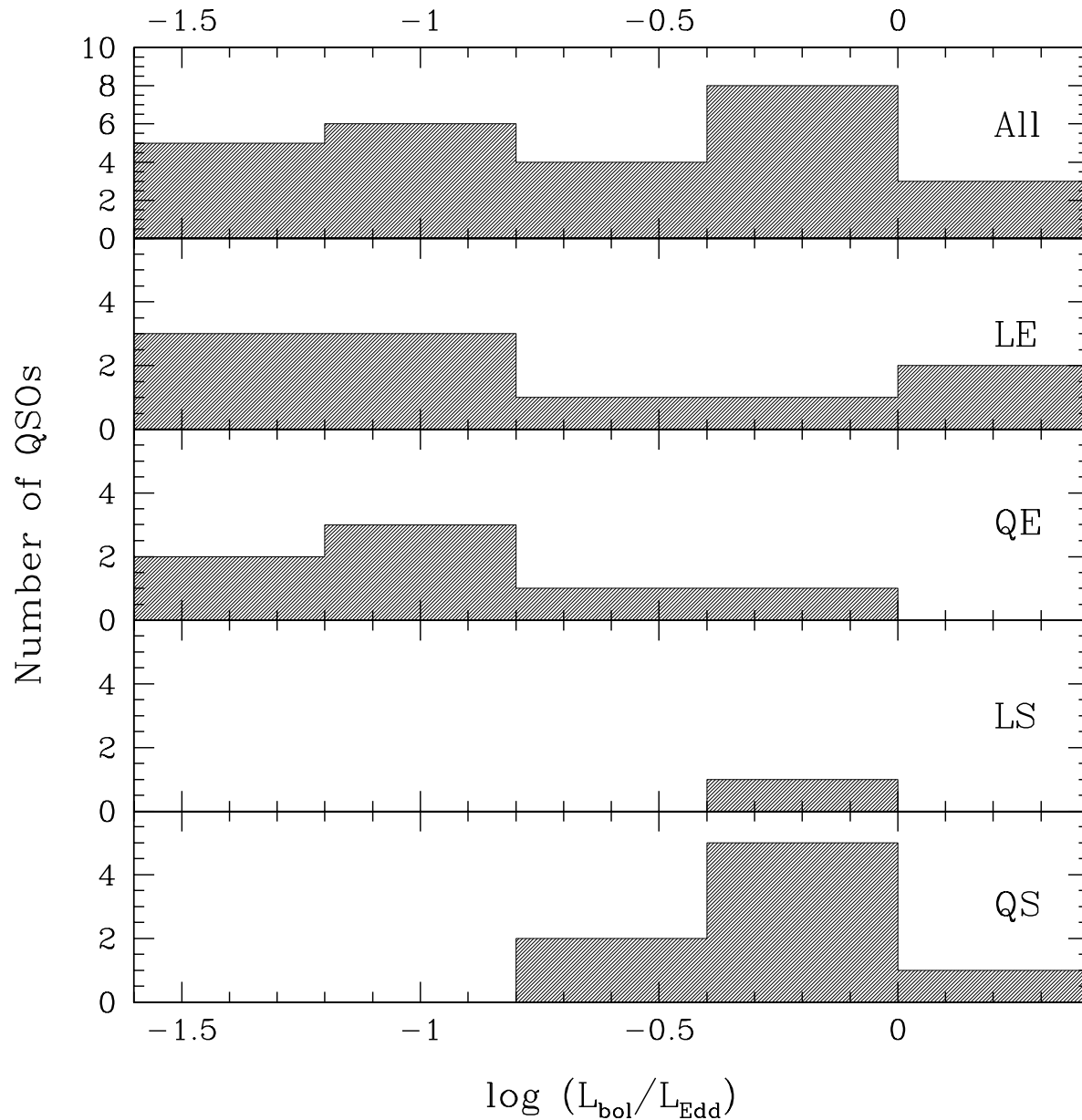


Fig. 4.— Distributions of Eddington fractions, with a bin width of 0.4 (equal to the uncertainties) and subdivided by morphology and radio loudness. The spirals tend to cluster at high Eddington fractions, while the ellipticals are spread over a wide range. Note the different vertical scale used for the complete sample’s plot.

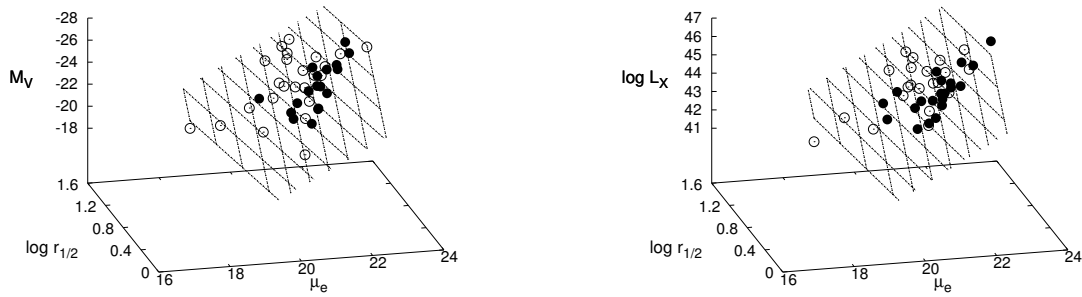


Fig. 5.— Views of the optical (left) and x-ray (right) QSO fundamental planes, showing the individual QSOs (filled and open circles) and the plane (grid) fitted to the overall sample. The host properties are the horizontal axes, while nuclear luminosity is vertical. In both cases, nuclear luminosity increases upward. The plots are viewed from above the plane; filled circles lie above the plane, and open circles lie below.

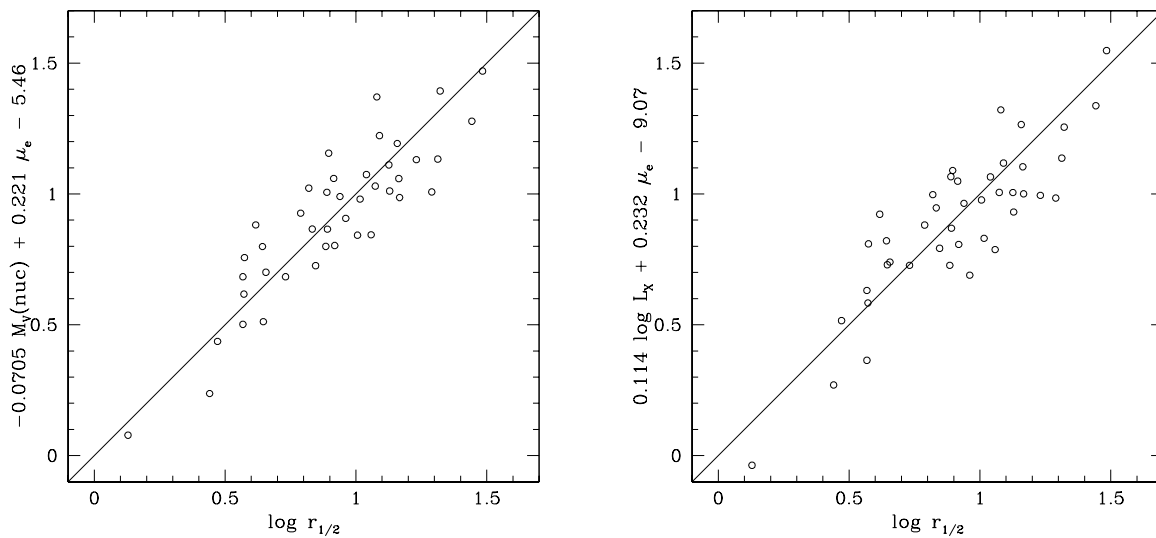


Fig. 6.— Overall QSO fundamental plane (vertical axis), plotted against the measured host galaxy size ($\log r_{1/2}$, horizontal axis). Points on the diagonal line show perfect correspondence. The left figure uses the QSO fundamental plane in its optical form, while the right figure uses the x-ray form. The QSO fundamental plane is most precise when solved for the host size.

Table 1. Observations and Data

Name (1)	z (2)	m_{nuc} (3)	m_{host} (4)	$M_V(\text{nuc})$ (5)	$M_V(\text{host})$ (6)	Morphology (7)	Radio (8)	Selection (9)
LBQS 0020+0018	0.423	19.30	19.34	-22.45	-22.77	E	Q	A
LBQS 0021-0301	0.422	19.03	19.10	-22.74	-23.03	E	Q	A
PG 0043+039	0.385	16.04	19.03	-25.49	-22.67	E	Q	B
PG 0052+251	0.155	16.04	16.83	-23.80	-23.08	S	Q	
PHL 909	0.171	15.97	16.89	-24.07	-23.29	E	Q	
UM 301	0.393	17.66	19.44	-23.92	-22.44	E	Q	A
3C 47	0.425	17.82	18.75	-24.07	-23.37	E	L	
3C 48	0.367	15.74	16.18	-25.72	-24.83	EI	L	
PHL 1093	0.26	17.21	17.17	-23.47	-23.54	E	L	B
MRK 1014	0.163	16.17	14.75	-23.30	-24.34	S ^a	Q	
PKS 0202-76	0.389	16.67	18.72	-24.98	-23.12	E	L	
NAB 0205+02	0.155	15.40	18.08	-24.37	-21.77	S	Q	
Q 0244+194	0.176	16.80	17.54	-23.29	-22.47	E	Q	
US 3498	0.115	19.30	15.87	-19.79	-23.10	S	Q	B
PKS 0312-77	0.223	16.13	16.67	-24.40	-23.78	E	L	
Q 0316-346	0.260	16.21	18.08	-24.68	-23.03	IS	Q	
3C 93	0.357	18.58	18.49	-23.51	-23.73	E	L	
IR 0450-2958	0.286	15.40	17.17	-25.41	-23.65	SI	Q	
PKS 0736+01	0.191	16.30	16.70	-24.03	-23.58	E	L	
MS 07546+3928	0.096	14.26	14.37	-24.22	-23.47	E	Q	
IR 0759+6508	0.149	15.94	15.65	-23.57	-23.73	SI	Q	
MS 0801.9+2129	0.118	16.00	15.66	-22.91	-22.80	S	Q	
3C 206	0.198	16.07	16.90	-24.03	-23.09	E	L	
3C 215	0.412	17.71	18.23	-24.08	-23.08	E	L	
PG 0923+201	0.19	15.53	17.46	-24.73	-23.00	E	Q	
MS 0944.1+1333	0.131	14.89	15.93	-24.16	-22.52	E	Q	
PG 0953+414	0.234	15.17	17.21	-25.23	-23.22	S	Q	B
PG 1001+291	0.330	15.59	17.90	-25.58	-23.33	S	Q	B
PKS 1004+13	0.24	15.15	17.00	-25.62	-24.06	E	L	
PG 1012+008	0.185	16.22	16.76	-23.75	-23.19	SI	Q	B
HE 1029-1401	0.086	13.84	15.86	-24.79	-22.74	E	Q	B
MS 1059.0+7302	0.089	16.60	15.41	-21.65	-22.34	S	Q	
PG 1116+215	0.177	14.85	16.74	-25.19	-23.42	S	Q	B
PG 1202+281	0.165	16.85	17.39	-23.03	-22.62	E	Q	B
LBQS 1209+1259	0.418	19.35	19.38	-22.39	-22.71	E	Q	A
PG 1216+069	0.331	15.42	18.70	-25.76	-22.55	E	Q	
LBQS 1218+1734	0.444	18.33	19.01	-23.54	-23.26	E	L	A
MS 1219.6+7535	0.071	15.06	14.56	-22.72	-22.52	ED	Q	
LBQS 1222+1010	0.398	18.38	18.62	-23.23	-23.24	S	Q	
LBQS 1222+1235	0.412	17.68	18.25	-24.04	-23.82	E	L	A
3C 273	0.158	12.60	15.65	-27.19	-24.24	E	L	
PG 1229+204	0.064	15.37	15.04	-22.27	-22.33	S	Q	C
LBQS 1240+1754	0.458	17.98	19.31	-23.93	-23.02	E	Q	A
LBQS 1243+1701	0.459	18.45	18.44	-23.49	-23.91	E	Q	A
3C 277.1	0.321	17.97	18.35	-23.09	-22.76	S	L	
PG 1302-102	0.278	15.19	17.35	-25.93	-24.14	E	L	
PG 1307+085	0.155	15.46	17.47	-24.33	-22.42	E	Q	B
PG 1309+355	0.184	15.56	16.61	-24.53	-23.62	S	L	
PG 1358+04	0.427	15.96	18.02	-25.84	-24.02	E	Q	B
Q 1402+436	0.323	15.15	17.42	-25.93	-23.73	EI	Q	
PG 1402+261	0.164	15.73	17.33	-24.12	-22.62	S	Q	
MS 1416.3-1257	0.129	15.83	16.90	-23.37	-21.70	E	Q	
B2 1425+267	0.366	15.88	17.47	-25.49	-23.45	E	L	
MS 1426.5+0130	0.086	14.30	14.49	-23.87	-23.17	S	Q	
PG 1444+407	0.267	15.80	17.37	-25.14	-23.81	S	Q	B
B2 1512+37	0.371	16.04	17.31	-25.38	-23.66	E	L	
MS 1519.8-0633	0.083	16.01	15.07	-22.32	-22.75	S	Q	
3C 323.1	0.264	16.07	18.01	-24.94	-23.33	E	L	B
MC 1548+114A	0.436	18.27	19.92	-23.66	-22.20	SI	L	
MC 1635+119	0.146	18.12	16.73	-21.38	-22.62	E	Q	
3C 351	0.372	15.50	16.97	-25.96	-24.59	S	L	
PKS 2135-147	0.200	16.21	16.91	-23.96	-23.23	E	L	
OX 169	0.211	15.89	17.28	-24.59	-23.18	EI	L	
MS 2159.5-5713	0.083	17.14	15.01	-20.91	-22.52	S	?	
Q 2201+315	0.295	15.46	16.75	-25.78	-24.50	E	L	
LBQS 2214-1903	0.396	18.81	19.27	-22.81	-22.60	S	Q	A
Q 2215-037	0.242	18.69	17.38	-22.06	-23.29	E	Q	

Table 1—Continued

Name (1)	z (2)	m_{nuc} (3)	m_{host} (4)	$M_V(\text{nuc})$ (5)	$M_V(\text{host})$ (6)	Morphology (7)	Radio (8)	Selection (9)
PKS 2247+14	0.237	16.65	17.22	-23.90	-23.32	E	L	
Q 2344+184	0.138	20.22	16.68	-19.16	-22.60	S	Q	
PKS 2349-014	0.174	15.97	15.63	-23.82	-24.07	IE	L	

Note. — Col. (3), apparent nuclear magnitude in filter. Col. (4), apparent host magnitude in filter. Col. (5), absolute V nuclear magnitude. Col. (6), absolute V host magnitude. Col. (7), host morphology: a) E=elliptical; b) S=spiral; c) EI=elliptical undergoing strong interaction; d) SI=spiral undergoing strong interaction; e) ED=elliptical with possible inner disk; f) IE=irregular or interacting that is best fit with an elliptical model; g) IS=irregular or interacting that is best fit with a spiral model. Col. (8), radio-loudness: Q = radio-quiet; L = radio-loud; ? = radio-loudness not available. Col. (9), original proposal selections: A = chosen from LBQS catalog; B = chosen from an optically-selected catalog; C = chosen for lack of extended host in ground-based images.

^aClassified here as spiral because it has a small central bulge on top of a larger component with apparently tidal arms. However, the tidal structure shows a de Vaucouleurs profile, and others (e. g., McLure et al. 1999) classify it as elliptical.

Table 2. PCA Subsample

Name	$\log r_{1/2}$	$\sigma_{\log r_{1/2}}$	μ_e	σ_{μ_e}	M_V (bulge)	σ_{M_V} (bulge)	M_V (nuc)	σ_{M_V} (nuc)	$\log L_X$	$\sigma_{\log L_X}$	X-ray Ref.
(1)	(2)	(3)	(4)	(5)	(6)	(7)	(8)	(9)	(10)	(11)	(12)
LBQS 0020+0018	0.471	0.024	19.52	0.13	-22.77	0.06	-22.45	0.15	44.36	0.13	1
PHL 909	0.919	0.005	20.66	0.07	-23.29	0.06	-24.07	0.14	44.60	0.05	1
UM 301	0.643	0.045	20.69	0.24	-22.44	0.08	-23.92	0.15	44.66	0.08	1
3C 47	0.731	0.023	20.12	0.14	-23.37	0.08	-24.07	0.15	44.99	0.02	2
3C 48	1.290	0.004	21.06	0.10	-24.83	0.10	-25.72	0.14	45.34	0.01	2
PHL 1093	1.164	0.006	22.01	0.07	-23.54	0.06	-23.47	0.15	44.45	0.01	2
PKS 0202-76	0.572	0.013	19.53	0.12	-23.12	0.10	-24.98	0.14	44.93	0.09	2
Q 0244+194	0.889	0.012	21.83	0.09	-22.47	0.06	-23.29	0.15	44.49	0.03	1
PKS 0312-77	1.313	0.003	22.05	0.08	-23.78	0.08	-24.40	0.14	44.66	0.07	2
3C 93	0.441	0.025	18.28	0.15	-23.73	0.08	-23.51	0.17	44.73	0.04	3
IR 0450-2958	0.896	0.010	21.83	0.15	-22.51	0.14	-25.41	0.14	44.70	0.02	2
PKS 0736+01	1.074	0.005	21.70	0.06	-23.58	0.06	-24.03	0.14	44.22	0.03	2
MS 07546+3928	0.568	0.007	19.25	0.10	-23.47	0.10	-24.22	0.15	43.58	0.15	2
IR 0759+6508	0.961	0.004	21.29	0.14	-23.34	0.13	-23.57	0.14	42.28	0.15	2
MS 0801.9+2129	0.568	0.012	20.49	0.17	-22.13	0.16	-22.91	0.14	43.40	0.22	1
3C 206	1.484	0.020	23.69	0.13	-23.09	0.08	-24.03	0.15	44.93	0.04	2
3C 215	0.891	0.047	20.94	0.25	-23.08	0.10	-24.08	0.14	44.57	0.03	2
PG 0923+201	1.090	0.010	22.35	0.10	-23.00	0.08	-24.73	0.14	43.88	0.14	1
MS 0944.1+1333	0.789	0.009	21.19	0.11	-22.52	0.10	-24.16	0.14	44.17	0.07	1
PG 1012+008	0.939	0.040	21.61	0.31	-22.64	0.24	-23.75	0.15	44.04	0.13	1
HE 1029-1401	0.915	0.004	21.59	0.08	-22.74	0.07	-24.79	0.14	44.83	0.01	1
PG 1202+281	0.656	0.006	20.53	0.10	-22.62	0.09	-23.03	0.15	44.27	<0.01	1
PG 1216+069	1.080	0.035	22.69	0.25	-22.55	0.17	-25.76	0.14	44.98	0.01	2
LBQS 1222+1235	1.167	0.018	21.50	0.11	-23.82	0.06	-24.04	0.14	44.58	0.02	1
3C 273	1.126	0.007	21.06	0.10	-24.24	0.10	-27.19	0.14	45.52	<0.01	2
PG 1229+204	0.833	0.009	21.52	0.15	-22.45	0.14	-22.27	0.14	44.07	0.01	4
PG 1302-102	1.129	0.008	21.01	0.10	-24.14	0.09	-25.93	0.14	44.97	0.01	2
PG 1307+085	0.820	0.010	21.57	0.11	-22.42	0.10	-24.33	0.15	44.41	0.01	2
MS 1416.3-1257	0.617	0.016	21.24	0.13	-21.70	0.10	-23.37	0.14	44.43	0.01	2
B2 1425+267	1.322	0.006	22.88	0.10	-23.45	0.10	-25.49	0.14	44.01	0.03	2
PG 1444+407	0.129	0.046	17.04	0.35	-22.96	0.26	-25.14	0.15	44.56	0.02	2
MS 1519.8-0633	0.574	0.039	21.01	0.31	-21.42	0.24	-22.32	0.15	43.90	0.11	1
3C 323.1	1.040	0.010	21.61	0.09	-23.33	0.08	-24.94	0.14	44.93	0.01	2
MC 1635+119	0.846	0.004	21.17	0.06	-22.62	0.06	-21.38	0.15	43.43	0.12	2
3C 351	1.016	0.012	20.86	0.16	-24.01	0.15	-25.96	0.14	44.39	0.52	2
PKS 2135-147	1.158	0.007	22.46	0.07	-23.23	0.06	-23.96	0.15	44.95	0.02	2
OX 169	0.885	0.003	20.48	0.13	-23.21	0.12	-24.59	0.14	44.26	0.03	2
Q 2201+315	1.058	0.006	20.30	0.08	-24.50	0.08	-25.78	0.14	45.16	0.04	2
Q 2215-037	1.006	0.004	21.48	0.08	-23.29	0.08	-22.06	0.15	44.42	0.13	1
PKS 2247+14	1.231	0.004	22.20	0.07	-23.32	0.06	-23.90	0.14	43.11	0.09	2
Q 2344+184	0.646	0.013	20.91	0.15	-22.11	0.14	-19.16	0.29	43.5	0.1	5
PKS 2349-014	1.443	0.003	22.89	0.06	-24.07	0.06	-23.82	0.15	44.71	0.03	2

Note. — For elliptical hosts, we take the entire host as the “bulge.” For other host types, the bulge is the spheroidal component. Col. (2), half-light radius of host bulge (kpc). Col. (4), effective surface magnitude of host bulge (mag arcsec⁻²). Col. (6), absolute V magnitude of host bulge. Col. (10), 0.5 keV x-ray luminosity of nucleus (erg s⁻¹).

References. — X-ray literature; (1) Yuan et al. 1998; (2) Brinkmann et al. 1997; (3) Wilkes et al. 1994; (4) Grupe et al. 2001; (5) Margon et al. 1985.

Table 3. Correlations and Linear Fits

Dependent	Independent	Subsample	N_{obj}	ρ	Probability	Slope	σ_{slope}	Intercept	$\sigma_{\text{intercept}}$
$M_V(\text{host})$	$M_V(\text{nuc})$	All	56	0.350	0.01	0.30	0.09	-15.9	2.2
		LE	22	0.434	0.04	0.29	0.08	-16.6	1.9
		QE	16	0.394	0.13	0.26	0.17	-16.7	4.2
		LS	4	0.800	0.20	0.77	0.14	-4.5	3.5
		QS	14	0.002	0.99	-0.03	0.16	-23.9	4.0
		L	26	0.578	<0.01	0.39	0.09	-14.1	2.2
		Q	30	0.168	0.37	0.14	0.14	-19.6	3.4
		E	38	0.379	0.02	0.32	0.10	-15.4	2.5
		S	18	0.315	0.20	0.25	0.17	-17.1	4.3
$M_V(\text{bulge})$	$\log(\mathcal{M}_{\text{BH}}/\mathcal{M}_{\odot})$	All	20	-0.263	0.26	-1.43	1.18	-10.5	10.5
		LE	10	0.103	0.78	-0.57	0.92	-18.6	8.2
		QE	7	-0.847	0.02	-1.86	1.41	-6.1	12.5
		LS	1
		QS	2	0.16	<0.01	-24.1	0.1
		L	11	0.059	0.86	-0.47	0.73	-19.4	6.5
		Q	9	-0.594	0.09	-1.31	1.12	-11.2	9.8
		E	17	-0.217	0.40	-1.64	1.91	-8.6	17.2
		S	3	-0.500	0.67	0.19	0.14	-24.7	1.1
$M_V(\text{nuc})$	$\log(\mathcal{M}_{\text{BH}}/\mathcal{M}_{\odot})$	All	26	-0.378	0.06	-1.98	1.16	-6.9	10.2
		LE	10	-0.164	0.65	-2.75	4.09	0.1	37.0
		QE	7	-0.536	0.22	-5.16	4.98	22.4	44.8
		LS	1
		QS	8	-0.643	0.09	3.05	4.03	-50.1	33.9
		L	11	-0.196	0.56	-2.27	2.23	-4.4	20.0
		Q	15	-0.318	0.25	-1.72	1.64	-9.2	14.3
		E	17	-0.472	0.06	-4.33	4.31	14.7	38.9
		S	9	-0.667	0.05	2.09	2.19	-42.0	18.4

Note. — For elliptical hosts, we take the entire host as the “bulge.” For other host types, the bulge is the spheroidal component. These correlations include only those objects for which $M_V(\text{nuc}) \leq -23.0$. The number of objects in each sample varies from one test to another, according to the available data. Col. (4), number of objects in subsample. Col. (5), Spearman rank correlation coefficient. Col. (6), the significance, listed as the probability that $|\rho|$ could be this large or larger by chance alone. Fits are of the form $\text{Dependent} = \text{slope} \times \text{Independent} + \text{intercept}$.

Table 4. Black Hole Masses, Eddington Fractions, and Bulge Magnitudes

Name	$\log \mathcal{M}_{\text{BH}}/\mathcal{M}_{\odot}$	$\log L_{\text{bol}}/L_{\text{Edd}}$	$M_V(\text{bulge})$	$\sigma_{M_V(\text{bulge})}$
PG 0052+251	8.8	-0.8
PHL 909	9.4	-1.4	-23.29	0.06
PHL 1093	9.1	-1.3	-23.54	0.06
MRK 1014	8.2	-0.5
NAB 0205+02	8.3	-0.2
Q 0244+194	8.5	-0.8	-22.47	0.06
PKS 0736+01	8.5	-0.5	-23.58	0.06
PG 0923+201	9.4	-1.1	-23.00	0.08
PG 0953+414	8.9	-0.4
PKS 1004+13	9.6	-0.9	-24.06	0.12
PG 1012+008	8.3	-0.4	-22.64	0.24
HE 1029–1401	9.6	-1.2	-22.74	0.07
PG 1116+215	8.7	-0.2
PG 1202+281	8.8	-1.2	-22.62	0.09
3C 273	9.1	0.2	-24.24	0.10
PG 1302–102	8.8	0.0	-24.14	0.09
PG 1307+085	8.3	-0.2	-22.42	0.10
PG 1309+355	8.5	-0.3	-23.62	0.17
PG 1402+261	7.8	0.3
PG 1444+407	8.5	-0.1	-22.96	0.26
3C 323.1	9.4	-1.0	-23.33	0.08
MC 1635+119	8.6	-1.6	-22.62	0.06
PKS 2135–147	9.4	-1.4	-23.23	0.06
OX 169	9.2	-1.0	-23.21	0.12
PKS 2247+14	8.1	-0.1	-23.32	0.06
PKS 2349–014	9.3	-1.3	-24.07	0.06

Note. — For elliptical hosts, we describe the entire host as the “bulge.” For other host types, the bulge is the spheroidal component. A standard deviation of 0.4 dex is used for all of the black hole masses, adopted from Vestergaard (2004). Since the errors in $M_V(\text{nuc})$ are much smaller, the propagated errors in $\log(L_{\text{bol}}/L_{\text{Edd}})$ all come out to be 0.4, as well.

Table 5. PCA Results

Type	Eigenvector	λ (%)	Cumulative %
Optical	e_1	63.4	63.4
	e_2	32.6	96.1
	e_3	3.9	100.0
X-Ray	e_1	61.7	61.7
	e_2	33.5	95.2
	e_3	4.8	100.0

Note. — Col. (3), eigenvalue as a percent of total variance. Col. (4), cumulative percentages.

Table 6. Fundamental Plane RMS Errors and Correlations

Variable	RMS Error	Correlation
	Optical	
$\log r_{1/2}$	0.139	0.883
μ_e	0.630	0.866
$M_V(\text{nuc})$	1.97	0.532
	X-ray	
$\log r_{1/2}$	0.156	0.855
μ_e	0.668	0.847
$\log L_X$	1.36	0.367

Note. — Optical fundamental plane results are listed first, and x-ray FP results follow. Col. (2), RMS differences between the measured variable and its FP solution. Col. (3), Pearson correlation coefficient between the measured variable and its FP solution.

Table 7. Comparison with the Literature

Name	Δm_{nuc}	Δm_{host}	$\Delta \log r_e$	Morphology	Reference
LBQS 0020+0018	-0.22	0.01	...	E	4
LBQS 0021–0301	-0.12	-0.77	...	E	4
PG 0043+039	-1.26	0.13	-0.547	E	2
PG 0052+251	...	-0.37	0.20	S ^a	1
PHL 909	...	-0.31	-0.018	E	1
UM 301	-0.15	-0.53	...	E	4
3C 48	...	-1.02	0.26	E	6
PHL 1093	-0.09	-0.03	0.045	E	7
PKS 0202–76	-1.23	-1.28	0.04	E	2
NAB 0205+02	...	-0.92	0.30	S ^a	1
Q 0244+194	0.00	0.04	-0.06	E	7
US 3498	-0.20	-0.03	0.065	S ^a	7
PKS 0312–77	-1.77	-1.03	0.068	E	2
PKS 0736+01	0.10	-0.20	-0.0496	E	7
PG 0923+201	...	-0.04	0.00	E	1
PKS 1004+13	...	0.10	0.15	E	1
HE 1029–1401	...	-0.34	0.08	E	1
PG 1202+281	...	-0.31	-0.056	E	1
LBQS 1209+1259	-0.21	-0.82	...	E	4
LBQS 1218+1734	-0.03	-0.62	...	E	4
LBQS 1222+1010	-0.08	-1.97	...	S	4
LBQS 1222+1235	-0.18	-0.60	...	E	4
3C 273	...	-0.35	0.0	E	1
PG 1229+204	-0.13	0.44	...	S ^b	5
LBQS 1240+1754	-0.15	-0.19	...	E	4
LBQS 1243+1701	-0.26	-2.40	...	E	4
PG 1302–102	...	-0.85	0.36	E	1
PG 1307+085	...	-0.33	0.18	E	1
PG 1309+355	...	-0.19	0.0	S ^c	1
PG 1358+04	-1.24	-1.78	... ^d	E	2
PG 1402+261	...	-0.97	0.04	S ^a	1
B2 1425+267	...	-0.13	0.11	E	6
3C 323.1	...	-0.09	0.11	E	1
MC 1635+119	0.02	-0.07	0.04	E	7
3C 351	-1.00	-2.23	0.43	S ^c	2
OX 169	-0.11	0.08	0.32	E ^e	7
LBQS 2214–1903	-0.17	-0.48	...	S	4
Q 2215–037	0.09	-0.82	0.28	E	3
PKS 2247+14	-0.25	0.02	0.201	E	7
Q 2344+184	1.02	-0.52	0.08	S ^a	7
PKS 2349–014	-0.03	-0.27	0.177	E	7

Note. — In each of columns (2), (3), and (4), the difference is calculated as our value - the literature value. Col. (2), difference in nuclear magnitude. Col. (3), difference in host magnitude. Col. (4), difference in log effective radius ($\log r_{1/2}$ for ellipticals or $\log r_{\text{eff}}$ for spirals). Col. (5), host morphology, quoted in its simplest form: E (elliptical) or S (spiral). The number of significant figures in the table varies with the precision of the literature values. Ellipses (...) are shown if no value is given. Values quoted from Bahcall et al. (1997) and Kirhakos et al. (1999) are their 2D model results.

References. — literature references; (1) Bahcall et al. (1997); (2) Boyce et al. (1998); (3) Disney et al. (1995); (4) Hooper et al. (1997); (5) Hutchings et al. (1994a); (6) Kirhakos et al. (1999); (7) McLure et al. (1999).

^aliterature size assumes a disk only, while we account for both a bulge (or bar) and a disk. For PG 0052+251, NAB 0205+02, and PG 1402+261, we mask the central bulge or bar and fit only the disk, whereas Bahcall et al. (1997) fit one exponential profile to the entire host. For Q 2344+184 and US 3498, we fit both bulge and disk separately and use our disk size here; McLure et al. (1999) fit one exponential profile to the entire host.

^bHutchings et al. (1994a) do not list a morphology.

^cSize is $r_{1/2}$. A de Vaucouleurs profile fits best, but we classify it as a spiral based

on appearance. We compare with the de Vaucouleurs model of Bahcall et al. (1997).

^dWe find the radial profile of PG 1358+04 to be a “broken” de Vaucouleurs profile with two different effective radii, so we do not compare $\log r_{1/2}$ here.

^eliterature size assumes a bulge model for the entire host. We use our bulge model size here but mask other features. For 3C 351, the bulge is surrounded by a ring feature that we mask from the fit but Boyce et al. (1998) include. For OX 169, bulge is crossed by a large, arm-like feature we mask from the fit; we do not know exactly which areas are fitted by McLure et al. (1999).

Table 8. PCA Results by Subsample

Sample (#)	Eigenvector	Optical		X-ray	
		λ (%)	Cumulative %	λ (%)	Cumulative %
LE (19)	e_1	63.6	63.6	66.1	66.1
	e_2	34.3	97.9	31.4	97.4
	e_3	2.1	100.0	2.6	100.0
QE (14)	e_1	69.4	69.4	67.1	67.1
	e_2	25.7	95.0	28.3	95.4
	e_3	5.0	100.0	4.6	100.0
QS (8)	e_1	65.8	65.8	69.5	69.5
	e_2	32.4	98.1	28.0	97.4
	e_3	1.9	100.0	2.6	100.0
L (20)	e_1	63.7	63.7	65.8	65.8
	e_2	34.2	97.9	31.6	97.4
	e_3	2.1	100.0	2.6	100.0
Q (22)	e_1	63.6	63.6	63.1	63.1
	e_2	33.0	96.6	33.3	96.3
	e_3	3.4	100.0	3.7	100.0
E (33)	e_1	64.5	64.5	61.1	61.1
	e_2	30.8	95.3	33.8	94.8
	e_3	4.7	100.0	5.2	100.0
S (9)	e_1	62.2	62.2	65.4	65.4
	e_2	35.4	97.7	30.0	95.5
	e_3	2.3	100.0	4.5	100.0

Note. — Col. (1), subsample and number of QSOs. Cols. (3) & (5), eigenvalue as a percent of total variance. Cols. (4) & (6), cumulative percentages.

Table 9. Coefficients for FP Forms

Sample	R_{coeff}	M_{coeff}	C
Optical			
All	-14.2	3.14	-77.5
LE	-14.7	3.14	-75.8
QE	108	-22.4	361
QS	-29.5	5.55	-118
L	-15.3	3.29	-78.3
Q	-44.9	8.53	-168
E	-14.1	3.13	-77.1
S	-19.1	3.79	-88.1
X-ray			
All	8.74	-2.03	79.3
LE	10.8	-2.39	84.1
QE	-11.8	2.55	0.0918
QS	-33.5	5.89	-54.9
L	11.4	-2.51	85.9
Q	-59.3	11.5	-151
E	8.14	-1.93	77.6
S	42.1	-8.36	186

Note. — Coefficients and constants for the fundamental plane equations: in the optical case, $M_V(\text{nuc}) = R_{\text{coeff}} \log r_{1/2} + M_{\text{coeff}} \mu_e + C$, and in the x-ray case, $\log L_X = R_{\text{coeff}} \log r_{1/2} + M_{\text{coeff}} \mu_e + C$.

Table 10. QSO FP Gradients

Sample	Gradient magnitude $ \nabla F $	Azimuth α (deg)
Optical		
All	6.49	151
Q	19.9	155
QS	13.1	155
S	8.52	154
L	6.95	152
LE	6.65	152
E	6.45	151
QE	48.7	-27
X-ray		
All	10.1	-30
S	47.0	-26
L	13.0	-29
LE	12.4	-29
E	9.46	-31
QE	13.4	152
QS	36.6	156
Q	65.9	154

Note. — Full sample results are given in boldface. The subsample QSO FPs are grouped by azimuth and ranked by magnitude. The gradients are unitless, while the azimuthal directions are measured in degrees counterclockwise from the $+i$ axis.